

# Topology optimization in B-spline space

Xiaoping Qian

Mechanical, Materials, and Aerospace  
Engineering Department  
Illinois Institute of Technology  
Chicago, IL 60662, USA  
Email: qian@iit.edu

## Highlights

- The density distribution is represented by B-splines over a rectangular domain.
- Through degrees and knot resolution control, optimized designs are free from checker-boards without extraneous filtering or penalty.
- The B-spline based density representation is independent from analysis elements, applicable to various analysis techniques and allows multi-resolution design without re-meshing.
- Compared with existing density filter based schemes, the B-spline based density representation is compact in storage and does not require neighboring element information.

**Abstract** In this paper, we present a new form of density based topology optimization where the design space is restricted to the B-spline space. An arbitrarily shaped design domain is embedded into a rectangular domain in which tensor-product B-splines are used to represent the density field. We show that, with proper choice of B-spline degrees and knot spans, the B-spline design space is free from checkerboards without extraneous filtering or penalty. We further reveal that the B-spline representation provides an intrinsic filter for topology optimization where the filter size is controlled by B-spline degrees and knot spans. This B-spline filter is effective in removing numerical artifacts and controlling minimal feature length in optimized structures when the B-spline basis functions span multiple analysis elements. We demonstrate that the B-spline filter is linear in storage cost and does not require neighboring element information. Further, this B-spline based density representation decouples the design representation of density distribution from the finite element mesh thus multi-resolution designs can be obtained without re-meshing the design domain. In particular, successive optimization with respect to design resolutions leads to topologically simple features obtainable in either coarse or fine design resolutions, thus achieving a form of mesh independency with respect to design representation. This approach is versatile in the sense a variety of finite element and isogeometric analysis techniques can be used for solution of equilibrium equations and a variety of projection methods can be used to approximate B-spline density in analysis. Numerical studies have been conducted over several representative topology optimization problems, including minimal compliance of MBB beams, compliant mechanism inverters, and heat conductions.

**Keywords** Topology optimization, B-splines, finite element, isogeometric analysis

# 1 Introduction

Topology optimization is a computational technique for optimally distributing materials in a design domain under governing physics. Its applications ranges from traditional mechanics applications [1] to fluids, heat transfer, electromagnetic and multiphysics applications [2]. Various methods for topology optimization have been developed. They include density distribution, level set, phase field, and evolutionary methods [2]. The density distribution based method is by far the most popular approach where the densities at the analysis elements or nodes are usually used as design variables to represent the density. One challenge in topology optimization is how to deal with numerical artifacts such as checkerboard and mesh dependencies [3]. The approaches to overcome numerical artifacts in topology optimization can be through relaxation of admissible set or restriction of admissible set. One way to enlarge the admissible design space is to allow an infinite perforation at a microscale. Global material properties can be obtained from such microstructures through homogenization [1, 2, 4]. An alternative is to restrict the design space so that in the restricted solution space the optimization problem is well-posed. One type of restriction approaches is to impose constraints on the design space and this includes bounds on the design gradients [5], slope constraints [6], and constraints on perimeters [7]. The other type of restriction includes the use of filters and penalty: sensitivity filters from Sigmund [8, 9], density filter [10, 11], regularized penalty [12], and Tikhonov-type regularization [13].

In this paper, we present a new form of density representation in the density distribution based topology optimization. We restrict the density distribution to be in the B-spline space. We embed an arbitrarily shaped design domain into a rectangular domain where tensor-product B-splines are used to represent the density distribution. We cast topology optimization as seeking optimal distribution of B-spline represented density where design variables are B-spline coefficients. Numerical studies have been conducted over several representative topology optimization problems, including minimal compliance of MBB beams, compliant mechanism inverters, and heat conductions. The salient features of such B-spline based density parametrization include

- *Design space can be free from checkerboard without extraneous filtering or penalty.* We show that, when the B-spline resolution is compatible with the underlying analysis resolution, the optimized designs are free from checkerboard. Our study further reveals that B-splines have inherent filtering effect with the effective filter size depending on the degrees and knots of the B-splines. Unlike the usual analysis elements based density representation, the B-spline based density representation is independent from analysis elements and thus the B-spline filter does not require information on density variables' neighboring analysis elements. Due to its tensor product nature, the B-spline filter is compact and can be computed on the fly, thus reduces the usual storage cost of cubic (or quadratic) order with respect to filter size to linear cost for three-dimensional (or two-dimensional) problems. Note, the classical density or sensitivity filter can be hugely expensive for large-scale three-dimensional problems since the required storage is proportional to  $(r/h)^3$  where the  $r$  is the filter radius and  $h$  is the element size. Thus, the B-spline filter provides an efficient filtering scheme similarly as partial differential equation (PDE) based filter [14, 15, 16], but without the need to solve the PDE.
- *Mesh independence.* Since the density is parameterized by finite number of B-spline coefficients, this ensures that the topology optimization is a finite-dimensional problem with optimized designs independent from analysis mesh resolution.

- *Multi-resolution design.* B-spline based design parametrization provides an easy means for multi-resolution design due to the readily available algorithms for B-spline refinement and the fact the B-spline domain does not need to be conformal to the underlying geometry. Multi-resolution designs can thus be obtained without re-meshing the design domain provided that the computational mesh for the analysis is sufficiently fine. Multi-resolution design allows design at coarse design resolution be used as initial designs for optimization at fine resolution, thus leads to topologically simple designs that are independent from design resolutions. Numerical results show that mesh independency with respect to design resolution can be achieved via such successive multi-resolution design optimization.
- *Separate design and analysis representation.* This B-spline based design parametrization of density distribution is independent from the analysis discretization of the design domain where a variety of analysis techniques can be used. This separation allows finite element discretization in topology optimization solely determined by desired accuracy in modeling the governing physics. It also allows the design resolution to be solely determined by the desired minimum length scale of features in the resulting design. In this paper, B-spline based topology optimization has been implemented in linear quadrilateral elements, triangular linear elements and NURBS based isogeometric analysis with density evaluated respectively at element center, element node, and quadrature points.

Our B-spline based density representation is based on our earlier work on B-spline based heterogeneous object modeling [17, 18, 19] where B-splines are used to represent both material composition and geometry and for solution of governing physical problems in multi-material or functionally gradient materials objects. Interestingly, an approach similar to this paper has been proposed in [20] where material representation in B-splines and geometry representation in implicit form have been used. Details on heterogeneous object modeling are available in a survey [21].

Our use of B-splines in topology optimization is different from other B-spline related approaches in topology optimization. In [22], trimmed B-spline surface analysis and isogeometric analysis are used for topology optimization where surface control points and trimming curves' control points are design variables and some selection criteria are used to generate internal holes. In [23], a phase-field approach is adopted for topology optimization and isogeometric analysis is used for geometric exactness of the design domain and for solution of phase field problems. In [24], B-spline finite elements are used in a density based approach to obtain topology that is free from checkerboard. In this approach, a penalization of density gradient is used to smooth the density and obtain mesh-independent solution. The use of B-splines as an implicit representation for shape optimization with topological control has been explored in [25]. It is also worth noting that, although the use of B-splines for density parametrization has not been explored much in topology optimization, in shape optimization the use of B-splines to avoid shape oscillation and to ensure existence of solution has been used as early as 1980s [26], and as recent as isogeometric shape optimization [27, 28].

Our approach is also different from wavelet approaches. Design parametrization in wavelet space has been explored in [29, 30]. However, wavelet representation cannot be used directly in topology optimization as it introduces a large number of constraints for enforcing the density constraints, thus reducing its computational efficiency. Instead, intermediate variables are mapped from density via the sigmoid function to variables in wavelet space in order to impose density box constraints [29]. In contrast, in our proposed approach, B-spline coefficients are directly used as design variables under simple box constraints.

In the remainder of this paper, Section 2 presents B-splines and its mathematical properties that are useful for topology optimization. Section 3 presents the optimization formulation for topology optimization in B-spline space. Section 4 analyzes the B-spline representation and shows B-spline is a filter with inherent length scale. Section 5 presents numerical results on topology optimization of MBB beams, compliant inverters and heat conduction. Section 6 shows results on topology optimization of curved design domains. This paper is concluded in Section 7.

## 2 B-splines

This section gives a brief introduction on B-splines. B-splines are commonly used in data approximation and in computer-aided geometric design. B-splines and non-uniform rational B-splines have become the standard representation in computer-aided design systems. Here, we introduce basic B-spline properties that are useful for topology optimization in this paper. For details on B-splines, refer to [31, 32].

A univariate B-spline function of degree  $p$  is defined as follows

$$f(x) = \sum_{i=0}^n B_{i,p}(x)b_i, \quad (1)$$

where  $\{b_i\}$  represents a set of  $i = 0, \dots, n$  B-spline coefficients. A degree  $p$  B-spline basis function  $\{B_{i,p}\}$  is defined on a knot vector  $\Xi = \{\bar{x}_0, \bar{x}_1, \dots, \bar{x}_{n+p+1}\}$ . A knot vector  $\Xi$  is a set of non-decreasing real numbers in parameter space. The interval  $[\bar{x}_i, \bar{x}_{i+1}]$  is called the  $i$ -th knot span. A knot vector is said to be uniform if its knots are uniformly spaced and otherwise non-uniform. In this paper, uniform B-splines are used. The  $i$ -th ( $i = 0, \dots, n$ ) B-spline basis function can be defined recursively as

$$B_{i,p}(x) = \frac{(x - \bar{x}_i)B_{i,p-1}(x)}{\bar{x}_{i+p} - \bar{x}_i} + \frac{(\bar{x}_{i+p+1} - x)B_{i+1,p-1}(x)}{\bar{x}_{i+p+1} - \bar{x}_{i+1}}, \quad (2a)$$

$$B_{i,0}(x) = \begin{cases} 1 & \bar{x}_i \leq x \leq \bar{x}_{i+1}, \\ 0 & \text{Otherwise.} \end{cases} \quad (2b)$$

B-spline basis functions have some important properties, including

- Local support: a  $p$ -th order B-spline function is non-zero in at most  $(p + 1)$  knot intervals.
- Non-negative and partition of unity, that is

$$B_{i,p}(x) \geq 0, \quad \sum_{i=0}^n B_{i,p}(x) = 1.$$

Figure 1 shows the B-spline basis functions for degree  $p = 1, 2, 3$  over the knot vector  $\Xi = \{0, 1, 2, 3, 4, 5, 6, 7, 8, 9, 10\}$ . The B-spline basis functions that span the knot interval  $[3, 3 + p + 1]$  are highlighted. It can be seen that a  $p$ -th degree B-spline function spans  $p + 1$  knot spans.

A tensor-product B-spline function of degree  $p$  in  $x$  direction and degree  $q$  in  $y$  direction is a bivariate piecewise polynomial function of the form

$$f(x, y) = \sum_{k=0}^n \sum_{l=0}^m B_{k,p}(x)B_{l,q}(y)b_{k,l},$$

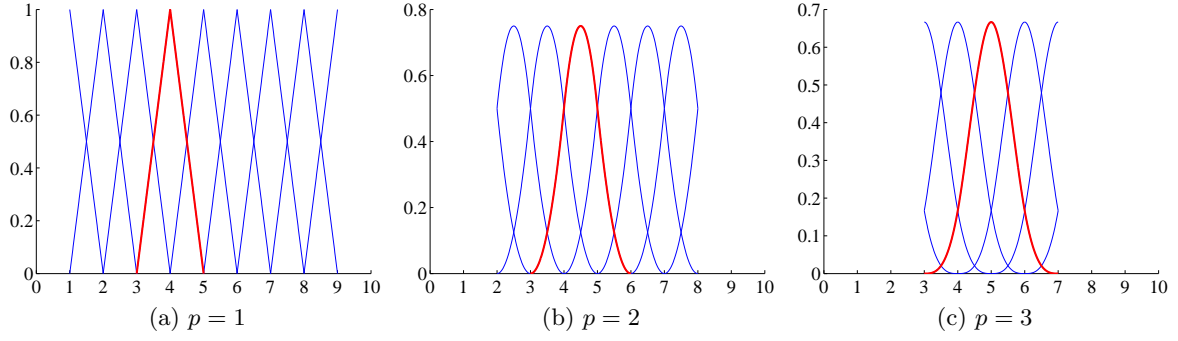


Figure 1: B-spline basis functions with degrees  $p = 1, 2, 3$  for knot vector  $\Xi = \{0, 1, 2, 3, 4, 5, 6, 7, 8, 9, 10\}$ . The B-spline basis functions that respectively span  $[3, 3 + p + 1]$  are highlighted.

where  $b_{k,l}$  form a  $(n + 1) \times (m + 1)$  B-spline coefficients for the function  $f(x, y)$ , and  $\{B_{k,p}\}$  and  $\{B_{l,q}\}$  are the B-spline basis functions defined on the knot vectors in  $x$  and  $y$  directions. Although the coefficients  $b_{k,l}$  are not customarily associated with any spatial coordinates, the function  $f(x, y)$  can be cast as a non-parametric (or explicit) B-spline geometry in parametric representation as

$$\mathbf{S}(x, y) = \begin{bmatrix} x \\ y \\ f(x, y) \end{bmatrix}.$$

The  $x, y$  coordinates of such B-spline coefficients are at *Greville abscissae*. More specifically,  $x_i$  of the  $i$ th B-spline coefficient is given by

$$x_i = \frac{1}{p}(\bar{x}_{i+1} + \bar{x}_{i+2} + \cdots + \bar{x}_{i+p}), \quad i = 0 \text{ to } n,$$

where  $\bar{x}_i$  are knots (with total  $n + p + 1$  knots) in  $x$  direction. The  $y$  coordinates of the B-spline coefficients are defined similarly. The points  $(x_k, y_l, b_{kl})$  are called control points of the function  $f(x, y)$ . Figure 2 shows the locations of B-spline coefficients (red points), the effective knot spans (black squares) in the domain of the B-spline function, and the knots in  $x, y$  directions (red lines).

Without loss of generality, we here consider a bivariate B-spline function on a knot-interval basis, defined by an array of  $(p + 1) \times (q + 1)$  B-spline coefficients. Note, the B-spline basis function has local influence property, i.e. within a given knot span, only  $(p + 1) \times (q + 1)$  number of non-zero basis functions. So the number of B-spline coefficients per B-spline knot interval is  $(p + 1) \times (q + 1)$ . The B-spline basis function  $N_{k,l}$  for the B-spline coefficient  $b_{k,l}$  ( $k = 0, \dots, n$  and  $l = 0, \dots, m$ ) can be written as

$$N_{k,l}(x, y) = B_{k,p}(x)B_{l,q}(y) \quad (3)$$

where  $p$  and  $q$  are degrees of the B-spline basis functions  $B_{k,p}$  and  $B_{l,q}$ . Figure 3 gives an illustration of a B-spline basis function in 2D where  $p = 3$  and  $q = 2$ . As can be seen from this figure, the shape function spans 4 knot intervals in  $x$  direction and 3 knot intervals in  $y$  directions.

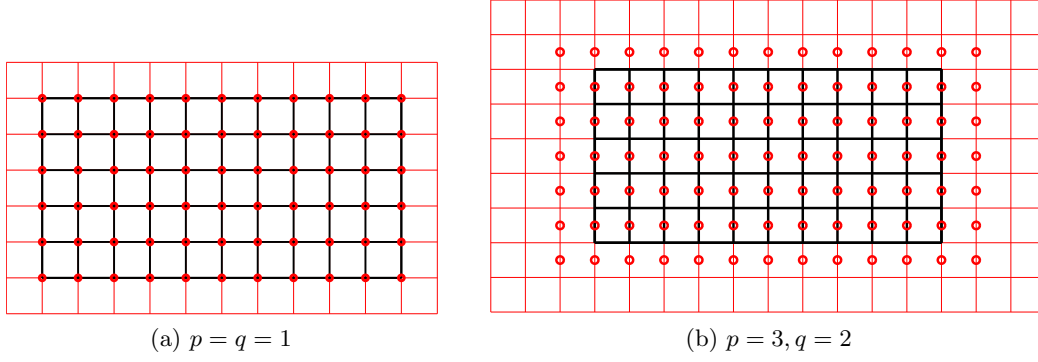


Figure 2: Control points for functions in B-spline form. Red lines represent knots, red circles represent the B-spline control points and black squares represent the domain of the function partitioned into knot spans.

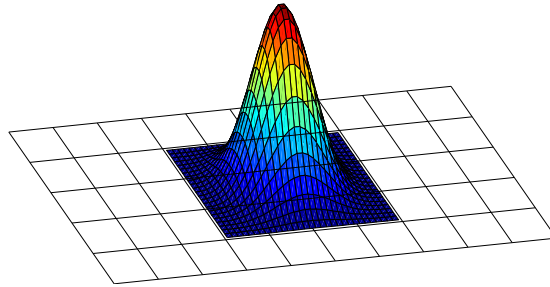


Figure 3: A tensor product B-spline basis function with degrees  $p = 3$  and  $q = 2$ , spanning  $(p + 1) \times (q + 1)$  knot intervals.

### 3 Topology optimization in B-spline space

In this section, we first give an algebraic description of optimization formulation with density field restricted to the tensor-product B-spline space. We then show how sensitivity of the objective function and the volume constraint with respect to B-spline coefficients can be derived.

#### 3.1 Continuous formulation of topology optimization in B-spline space

We give the formulation for the minimal compliance problem. The basic idea of our approach, as shown in Fig. 4, is to embed an arbitrarily shaped design domain  $\Omega$  into a B-spline function domain  $\bar{\Omega}$ . This B-spline function  $\tilde{\rho}(\mathbf{x}), \mathbf{x} \in \bar{\Omega}$ , represents the density distribution that are parameterized by a finite number of B-spline coefficients  $\rho_i$ .

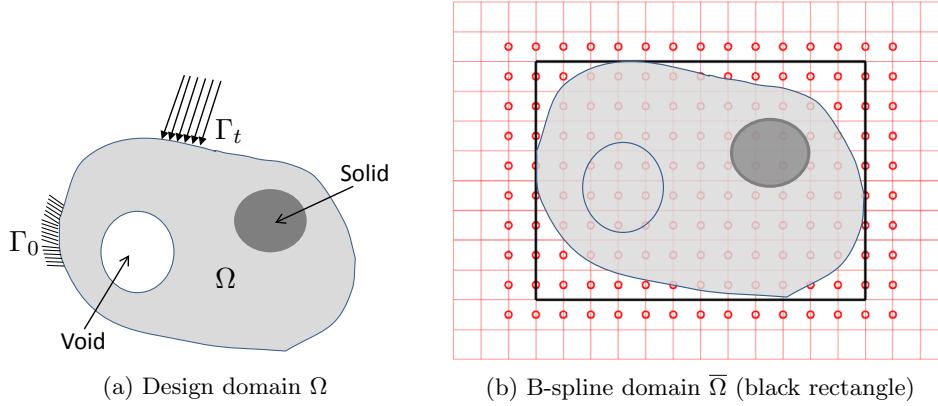


Figure 4: The design domain  $\Omega$  is embedded into a B-spline domain  $\bar{\Omega}$  where  $\Omega \subseteq \bar{\Omega}$ .

For a given design domain  $\Omega$ , the minimal compliance problem can be stated as finding the optimal distribution of stiffness tensor  $E_{ijkl}$  [2]. With the energy bilinear form

$$a_E(u, v) = \int_{\Omega} E_{ijkl} \varepsilon_{ij}(u) \varepsilon_{kl}(v) \, d\Omega,$$

and the load linear form

$$l(u) = \int_{\Omega} f u \, d\Omega + \int_{\Gamma_t} t u \, d\Gamma,$$

the minimal compliance problem can be stated as

$$\begin{cases} \min_{u \in U, E} & l(u) \\ \text{s.t.} & a_E(u, v) = l(v), \forall v \in U \\ & E \in E_{ad} \end{cases} \quad (4)$$

where the equilibrium equation is written in the weak, variational form with  $U$  denoting its kinematically admissible displacement field and  $\alpha_E$  depends on the stiffness tensor  $E$ . With the SIMP

formulation, the set of admissible stiffness tensor can be written as

$$E_{ijkl}(\mathbf{x}) = \tilde{\rho}(\mathbf{x})^s E_{ijkl}^0, \quad s > 1, \quad (5a)$$

$$\int_{\Omega} \tilde{\rho}(\mathbf{x}) \, d\Omega \leq V^*, \quad \mathbf{x} \in \Omega, \quad \Omega \subseteq \bar{\Omega} \quad (5b)$$

$$\tilde{\rho}(\mathbf{x}) = \sum_i N_i(\mathbf{x}) \rho_i, \quad 0 \leq \rho_i \leq 1, \quad \mathbf{x} \in \bar{\Omega} \quad (5c)$$

where  $\tilde{\rho}(\mathbf{x})$  is the desired distribution of density over a rectangular domain  $\bar{\Omega}$ ,  $s$  is the penalty factor and  $V^*$  is the allowed material volume. The design domain  $\Omega$  is embedded into the domain of the B-spline function and is a subset of the B-spline domain  $\bar{\Omega}$  (the black box in Fig. 4). Although the density function is defined over the B-spline domain  $\bar{\Omega}$ , the volume constraint (5b) and equilibrium equation (4) are imposed on the design domain  $\Omega$ . The continuous density function  $\tilde{\rho}(\mathbf{x})$  is parameterized by a finite set of B-spline coefficients  $\rho_i$ . Due to the partition of unity and non-negative properties of B-spline basis functions, the density is bounded between 0 and 1, i.e.  $0 \leq \tilde{\rho}(\mathbf{x}) \leq 1$  since each B-spline coefficient  $\rho_i$  is bounded within  $[0, 1]$  as shown in (5c).

The design representation of density is through B-splines  $\tilde{\rho}(\mathbf{x})$  defined over the rectangular domain  $\bar{\Omega}$  with design resolutions controlled by the number of knots and degrees. In practice, the B-spline domain can be constructed from the bounding box of the design domain as  $[x_{\min}, x_{\max}] \times [y_{\min}, y_{\max}]$ . This rectangular domain is then partitioned into  $m_x \times m_y$  knot intervals with additional  $p + 1$  (and  $q + 1$ ) knots in two ends of  $x$  (and  $y$ ) direction. In this paper, we are using uniform B-splines so all knots are uniformly distributed. There are  $(m_x + p) \times (m_y + q)$  B-spline coefficients  $\rho_i$  as design variables. Thus, we have a finite dimensional optimization problem: seeking a material density distribution  $\tilde{\rho}(\mathbf{x})$  that minimizes the compliance under the equilibrium constraint.

### 3.2 Discretized formulation

The continuous form of equilibrium equations in (4) is solved numerically, typically via finite element methods. The continuous B-spline represented density function  $\tilde{\rho}(\mathbf{x})$  thus needs to be approximated in each element. The approximation of density distribution  $\tilde{\rho}$  in each analysis element is noted as  $\bar{\rho}$ . The FE discretized version of the problem (4) with a given B-spline parameterization of density can be stated

$$\min_{\boldsymbol{\rho}, \mathbf{u}} \quad c(\bar{\boldsymbol{\rho}}) = \mathbf{f}^T \mathbf{u} \quad (6a)$$

$$\text{s.t.} \quad \mathbf{K}(\bar{\boldsymbol{\rho}}) \mathbf{u} = \mathbf{f} \quad (6b)$$

$$g(\bar{\boldsymbol{\rho}}) = \frac{\sum_{e \in N_e} \int_{\Omega^e} \bar{\rho}(\mathbf{x}) \, dv}{V_0} - \gamma \leq 0 \quad (6c)$$

$$0 \leq \rho_i \leq 1, \quad \forall i \in N_d \quad (6d)$$

where  $\boldsymbol{\rho}$  represent a set of B-spline coefficients,  $\bar{\boldsymbol{\rho}}(\mathbf{x})$  represents the analysis approximation of continuous density  $\tilde{\rho}(\mathbf{x})$ ,  $\mathbf{K}$  is the stiffness matrix of the underlying physical problem,  $\mathbf{u}$  and  $\mathbf{f}$  are the unknown state variables and force vector in finite element analysis,  $\int_{\Omega^e} \bar{\rho} \, dv$  is the volume of the analysis element  $e$ ,  $V_0 = \int_{\Omega} d\Omega$  is the volume of the design domain and  $\gamma$  is the allowed material volume fraction. The vector  $\mathbf{f}$  represents the force vector in minimal compliance design. The equation (6c) represents the volume constraint that is imposed on the approximate density



field  $\bar{\rho}$  that is used in FE analysis. The box constraints for the design variables in (6d) is that  $\rho_i \in [0, 1]$  due to the partition of unity and non-negative properties of B-spline basis functions so that the resulting density values  $\bar{\rho}$  is always within physically meaningful range  $[0, 1]$ . Note, this formulation is general and is applicable to other common optimization problems such as compliant mechanism and heat conduction problems. For the compliant inverter design, one can replace  $\mathbf{f}$  in the cost function with a zero vector at all DOFs except one at the output degree-of-freedom. For heat conduction, we change it to a scalar problem and replace  $\mathbf{f}$  in the cost function with a unit vector.

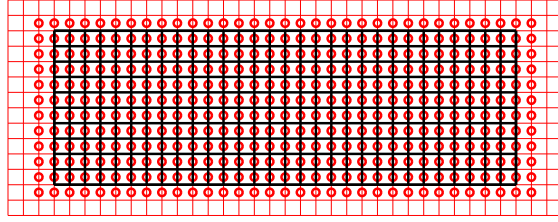
Our formulation is versatile in the sense that the B-spline density function  $\tilde{\rho}(\mathbf{x})$  can be applied in various analysis techniques and the density for analysis can be approximated in different ways. The B-spline based design representation of density is independent from how the physical domain is discretized in analysis elements. The density used in analysis  $\bar{\rho}(\mathbf{x})$  is simply evaluated from the design representation  $\tilde{\rho}(\mathbf{x})$  at location  $\mathbf{x}$ . In this paper, we demonstrate how three common methods can be used for approximating B-spline represented density distribution in finite element:

- *Element center based approximation* where element-wise constant density is used to approximate the density distribution  $\tilde{\rho}(x, y)$ . The density is typically evaluated at element center  $\mathbf{x}_e^c$ , representing the center of  $e$ -th element. Therefore, the element density is  $\bar{\rho}_e(\mathbf{x}) = \tilde{\rho}(\mathbf{x}_e^c)$ .
- *Node based approximation* where the density is evaluated from element nodes. That is,  $\bar{\rho}(\mathbf{x}) = \sum_k \tilde{\rho}(\mathbf{x}_k) N_k$  where  $\mathbf{x}_k$  represents the  $k$ -th node and  $N_k$  is the corresponding nodal shape function.
- *Gaussian quadrature based approximation* where the density is evaluated from quadrature points of the element. That is,  $\bar{\rho}_{e,j} = \tilde{\rho}(\mathbf{x}_{e,j}^q)$  where  $\mathbf{x}_{e,j}^q$  are element  $e$ 's  $j$ -th quadrature point. Each element can be viewed as being partitioned into cells with each cell corresponding to a quadrature point and cell areas proportional to the quadrature weights.

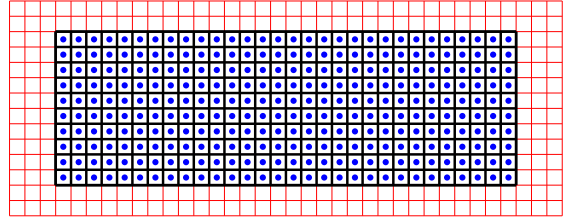
In all cases, the density distribution for analysis  $\bar{\rho}(\mathbf{x})$  approximates the B-spline represented density  $\tilde{\rho}(\mathbf{x})$  via the evaluation of the B-spline density function at points, either element centers  $\mathbf{x}_e^c$ , nodes  $\mathbf{x}_i^n$ , or quadrature points  $\mathbf{x}_{e,j}^q$ , in the B-spline domain.

Figure 5 gives a 2D and 3D view of the density distribution of an optimized design from degree  $p = 3, q = 2$  B-spline of  $30 \times 10$  knot intervals with analysis done by  $30 \times 10$  four-node quadrilateral linear elements. Although in this example, each element aligns with each knot span, they do not have to be in alignment in general. Figure 5a and Figure 5b present the distribution of B-spline coefficients  $\rho_i$ , densities  $\tilde{\rho}$  in element centers and the finite elements. Figure 5c plots the topological design with the distribution of piecewise constant density  $\bar{\rho}(\mathbf{x})$  in analysis elements. Figure 5d shows the 3D continuous distribution of density  $\tilde{\rho}(\mathbf{x})$  and the corresponding B-spline coefficients  $\{\rho_{k,l}\}$ . Figure 6 gives graphical illustrations of embedding design domains into B-spline domains for the use of the other two types of density evaluation points. In this figure, two additional element types are used: three-node linear triangular elements in a curved domain (Fig. 6a and b), and bi-quadratic NURBS elements for a curved design domain (Fig. 6c and d). In this figure, the red lines represent the knots and black outer bounds represent the B-spline domain  $\bar{\Omega}$ . In Fig. 6b, nodes from triangular mesh as shown in Fig. 6a are shown as blue dots in the B-spline domain  $\bar{\Omega}$ . In Fig. 6d,  $3 \times 3$  quadrature points for each bi-quadratic NURBS element in Fig. 6c are shown as blue dots in the B-spline domain.

Since the density distribution in each element can be approximated in various forms through  $\tilde{\rho}(\mathbf{x})$  at density evaluation points, the stiffness matrix and the material volume for each element



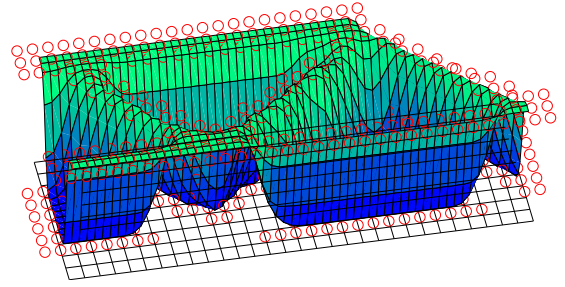
(a) Distribution of B-spline coefficients  $\rho_i$ .



(b) Q4 linear elements and element centers  $\mathbf{x}_e^c$ .

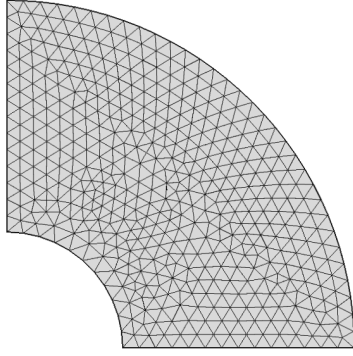


(c) Piecewise constant densities  $\bar{\rho}$  in analysis elements.

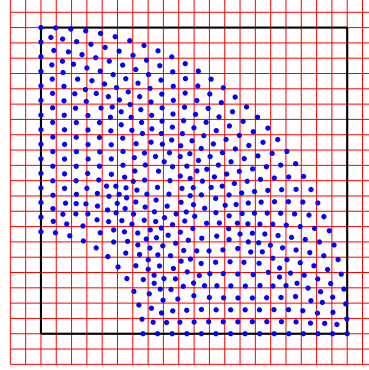


(d) 3D view of B-spline representation of the density distribution  $\tilde{\rho}(\mathbf{x}, y)$  and B-spline coefficients  $\rho_i$ .

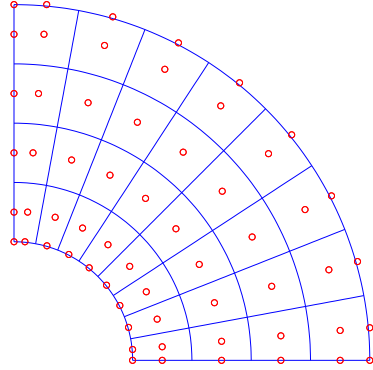
Figure 5: Optimized design and its density representation from degree  $p = 3, q = 2$  B-splines of  $30 \times 10$  knot intervals with analysis done by  $30 \times 10$  quadrilateral linear elements. (a) Distribution of  $33 \times 12$  B-spline coefficients  $\rho_i$  (red circle), (b) locations of  $30 \times 10$  density variables (blue dot)  $\tilde{\rho}(\mathbf{x}_e^c)$  in each element, and  $30 \times 10$  analysis elements (black square), (c) Piecewise constant densities  $\bar{\rho}(\mathbf{x})$  in analysis elements, (d) 3D view of density distribution  $\tilde{\rho}(\mathbf{x})$  and the B-spline coefficients  $\rho_{k,l}$ .



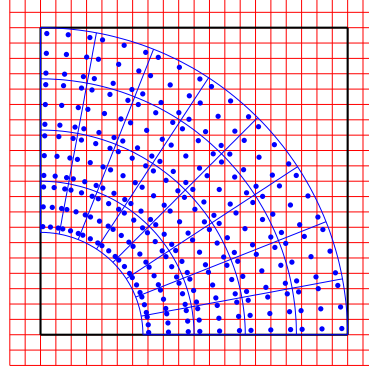
(a) Triangular mesh of a curved design domain



(b) Mesh nodes in B-spline domain



(c) NURBS discretization of a curved design domain



(d) Quadrature points in B-spline domain

Figure 6: Analysis elements are embedded into B-spline domains and element density approximated through density evaluation points. (a) and (b): Element density is approximated through nodal density where the density at each node is evaluated from the domain of bi-quadratic B-splines of  $20 \times 20$  knot spans. (c) and (d): Density in NURBS elements is approximated through density at quadrature points, which are embedded into the domain of bi-quadratic B-splines of  $20 \times 20$  knot spans.

can therefore be expressed through these density evaluation points. Generally, an element stiffness matrix is computed as follows

$$\mathbf{K}_e = \int_{\hat{\Omega}_e} \mathbf{B}(\mathbf{x})^T \mathbf{D}(\bar{\rho}) \mathbf{B}(\mathbf{x}) |\mathbf{J}(\mathbf{x})| d\hat{\Omega} \quad (7)$$

where  $\hat{\Omega}_e$  is the parametric domain of the element,  $\mathbf{D}(\bar{\rho})$  is the strain-stiffness matrix as a function of density  $\bar{\rho}$  in the element and  $\mathbf{J}$  is the Jacobian of the mapping from parametric integration domain to physical domain. In practice, the integral is done numerically by determining the value of the integrand at Gauss quadrature points in the element. We show below how the element stiffness matrix of the three approximations can all be expressed as algebraic equations consisting of density at the evaluation points  $\mathbf{x}^d$  where  $\mathbf{x}^d$  can be  $\mathbf{x}^c$ ,  $\mathbf{x}^n$  or  $\mathbf{x}^q$ . That is, the element stiffness matrix can be expressed as sum of terms evaluated at quadrature points  $\mathbf{x}_j$

$$\mathbf{K}_e = \sum_j E(\bar{\rho}(\mathbf{x}_j)) \mathbf{B}_j^T \mathbf{D}_0 \mathbf{B}_j |\mathbf{J}_j| \omega_j, \quad (8)$$

where  $\mathbf{D}_0$  is the stress-strain matrix for unit material and  $\omega_j$  is the weight for quadrature point  $j$  and  $E(\bar{\rho}(\mathbf{x}_j))$  is the material stiffness for quadrature point  $j$  in the element  $e$ . With the SIMP interpolation, the material stiffness can be expressed as

$$E(\bar{\rho}(\mathbf{x})) = E_{\min} + \bar{\rho}(\mathbf{x})^s (E_0 - E_{\min}) \quad (9)$$

where  $E_0$  is the stiffness of the solid phase,  $s$  is the penalization power, and  $\bar{\rho}(\mathbf{x})$  is the physical density in element  $e$  and  $E_{\min}$  is the minimal material stiffness to avoid singularity in stiffness matrix.

If  $\bar{\rho}$  is element-wise constant, all quadrature points have the same density as the B-spline density at element center, i.e.  $\bar{\rho}(\mathbf{x}_j) = \tilde{\rho}(\mathbf{x}^c)$ . Therefore the element stiffness matrix can be simplified as

$$\mathbf{K}_e = E(\tilde{\rho}(\mathbf{x}_e^c)) \sum_j \mathbf{B}_j^T \mathbf{D}_0 \mathbf{B}_j |\mathbf{J}_j| \omega_j = E(\tilde{\rho}(\mathbf{x}_e^c)) \mathbf{K}_e^0. \quad (10)$$

If  $\bar{\rho}$  is represented via nodal density  $\bar{\rho}(\mathbf{x}) = \sum_k \tilde{\rho}(\mathbf{x}_k^n) N_k(\mathbf{x})$  where each nodal density  $\tilde{\rho}(\mathbf{x}_k^n)$  is evaluated at each nodal position  $\mathbf{x}_k^n$  in the B-spline domain  $\hat{\Omega}$ , we have

$$\mathbf{K}_e = \sum_j \left( E_{\min} + \left( \sum_k \tilde{\rho}(\mathbf{x}_k^n) N_{k,j} \right)^s (E_0 - E_{\min}) \right) \mathbf{B}_j^T \mathbf{D}_0 \mathbf{B}_j |\mathbf{J}_j| \omega_j, \quad (11)$$

where  $N_{k,j}$  represents the node  $k$ 's shape function evaluated at element  $e$ 's  $j$ -th quadrature point.

If  $\bar{\rho}$  is represented via density at quadrature points  $\bar{\rho}_{e,j} = \tilde{\rho}(\mathbf{x}_{e,j}^q)$  where  $\mathbf{x}_{e,j}^q$  are element  $e$ 's  $j$ -th quadrature point. We have

$$\mathbf{K}_e = \sum_j \left( E_{\min} + \tilde{\rho}(\mathbf{x}_j^q)^s (E_0 - E_{\min}) \right) \mathbf{B}_j^T \mathbf{D}_0 \mathbf{B}_j |\mathbf{J}_j| \omega_j. \quad (12)$$

The material volume for each element can also be computed similarly. Generally, the volume for each element can be represented as  $V_e = \int_{\Omega_e} \bar{\rho}(\mathbf{x}) d\Omega$ . If the density is approximated element-wise constant, we have

$$V_e = \tilde{\rho}(\mathbf{x}^c) \sum_j |\mathbf{J}_j| \omega_j. \quad (13)$$

If the density is approximated via nodal density, we have

$$V_e = \sum_j |\mathbf{J}_j| \omega_j \sum_k \tilde{\rho}(\mathbf{x}_k^n) N_{k,j}. \quad (14)$$

If the density is approximated via quadrature points, we have

$$V_e = \sum_j |\mathbf{J}_j| \omega_j \tilde{\rho}(\mathbf{x}_j^q). \quad (15)$$

### 3.3 Sensitivity analysis

We use a gradient-based method for optimization. Thus the sensitivity of the cost function  $c$  and the volume constraint  $g$  with respect to the design variables, i.e. B-spline coefficient  $\rho_i$ , are needed. With the algebraic equations in the previous subsection describing the element stiffness matrix and element volume as functions of  $\tilde{\rho}(\mathbf{x}^d)$  at density evaluation points  $\mathbf{x}^d$ , it is not difficult to derive the sensitivity of the cost function and the volume constraint with respect to B-spline coefficients. Here we use the element-wise constant approximation as an example to show how analytical sensitivities can be readily derived.

The adjoint method can be used to compute the sensitivity of the objective function  $c$  with respect to design variables, i.e. B-spline coefficient  $\rho_i$ , as follows

$$\frac{\partial c}{\partial \rho_i} = \boldsymbol{\lambda}^T \frac{\partial \mathbf{K}}{\partial \rho_i} \mathbf{u}$$

where  $\boldsymbol{\lambda}$  is the adjoint vector determined from the adjoint equation  $\mathbf{K}\boldsymbol{\lambda} = -\mathbf{f}$ . Here  $\frac{\partial \mathbf{K}}{\partial \rho_i}$  can be obtained on an element level by differentiating (10)

$$\frac{\partial \mathbf{K}_e}{\partial \rho_i} = \frac{\partial \mathbf{K}_e}{\partial \tilde{\rho}(\mathbf{x}_e^c)} \frac{\partial \tilde{\rho}(\mathbf{x}_e^c)}{\partial \rho_i} = s(\tilde{\rho}(\mathbf{x}_e^c))^{s-1} (E_0 - E_{\min}) \mathbf{K}_e^0 \frac{\partial \tilde{\rho}(\mathbf{x}_e^c)}{\partial \rho_i}. \quad (16)$$

The density at the element center can be expressed as

$$\tilde{\rho}(\mathbf{x}_e^c) = \sum_{i \in I_{\mathbf{x}_e^c}} N_i(x_e^c, y_e^c) \rho_i \quad (17)$$

where  $(x_e^c, y_e^c)$  represents the coordinates of the center  $\mathbf{x}_e^c$  of the  $e$ -th element,  $I_{\mathbf{x}_e^c}$  is the indices of  $(p+1) \times (q+1)$  B-spline coefficient  $\rho_i$  that influences the density  $\tilde{\rho}(\mathbf{x}_e^c)$  and  $N_i$  is the B-spline shape function corresponding to the B-spline coefficient  $\rho_i$ . The index set  $I_{\mathbf{x}_e^c}$  depends on the position of  $\mathbf{x}_e^c$  with respect to the knot distribution of the B-spline representation. The sensitivity of  $\tilde{\rho}(\mathbf{x}_e^c)$  with respect to the design variable, i.e. B-spline coefficients  $\rho_i$ , is

$$\frac{\partial \tilde{\rho}(\mathbf{x}_e^c)}{\partial \rho_i} = N_i(x_e^c, y_e^c) \quad (18)$$

The  $N_i(x_e^c, y_e^c)$  is non-negative, thus leading to the monotonous increase of material stiffness with respect to the density. Plugging the above equation into (16) leads to the sensitivity of the cost function with respect to the B-spline coefficients  $\rho_i$ . The sensitivity of the volume constraint with respect to  $\rho_i$  can be computed similarly by using the chain rule of differentiation over (13).

Generally, the sensitivity of cost function and volume constraint essentially has two components, as shown in (16), the derivatives with respect to density  $\tilde{\rho}(\mathbf{x}^d)$  at evaluation points  $\mathbf{x}^d$  where  $\mathbf{x}^d$  is  $\mathbf{x}^c$  for element center,  $\mathbf{x}^n$  for nodal point, and  $\mathbf{x}^q$  for quadrature points, and the derivative of  $\tilde{\rho}(\mathbf{x}^d)$  with respect to B-spline coefficient  $\rho_i$ . The density  $\tilde{\rho}(\mathbf{x}^d)$  at each evaluation point is influenced by  $(p+1) \times (q+1)$  B-spline coefficients. The sensitivity with respect to  $\rho_i$  for such influence is  $N_i(\mathbf{x}^d)$ .  $N_i(\mathbf{x}^d)$  is constant for every  $\rho_i$ , thus it can be pre-stored before optimization. If an optimization problem has total  $M$  density evaluation points  $\mathbf{x}_l^d$ ,  $l = 1 \dots M$ , thus there are total  $M(p+1)(q+1)$  entries  $N_i(\mathbf{x}_l^d)$  to be pre-stored. This can become expensive, especially for 3D problems. Fortunately, for B-spline basis functions, due to their tensor product nature, the storage cost can be reduced significantly with negligible influence on the overall efficiency. For each density point  $\mathbf{x}_l^d$ , there are  $(p+1)(q+1)$  B-spline basis function  $N_{s,t}(\mathbf{x}_l^d)$ ,  $s = 1, \dots, p+1$ ,  $t = 1, \dots, q+1$ . Here  $s$  and  $t$  are matrix indices for the basis function  $N$ . Instead of directly storing these  $(p+1) \times (q+1)$  entries, for each density point  $\mathbf{x}_l^d$ , one can simply store  $p+1$  entries of  $B_s(x_l^d)$  and  $q+1$  entries of  $B_t(y_l^d)$  where  $B_s(x_l^d)$  and  $B_t(y_l^d)$  are respectively the B-spline basis function in  $x$  and  $y$  directions. Then the tensor-product B-spline basis function  $N_{s,t}(\mathbf{x}_l^d)$  can be dynamically reconstructed as

$$N_{s,t}(x_l^d, y_l^d) = B_s(x_l^d)B_t(y_l^d) \quad (19)$$

during each optimization iteration. That is, the tensor product form of B-spline basis function makes it possible for storing only  $M((p+1) + (q+1))$  entries instead of  $M(p+1)(q+1)$ , at the expense of computing the simple multiplication in (19) in each iteration. The sensitivities in all numerical examples in this paper are obtained this way. Such storage saving can be substantial for 3D problems. Although the equations are only shown here in 2D, it is directly applicable to 3D.

**Remark 1** *This tensor product form of B-splines reduces the quadratic (or cubic) storage cost of B-spline sensitivities with respect to B-spline degrees and knot spans to linear cost for 2D (or 3D) problems.*

**Remark 2** *The analysis density  $\bar{\rho}(\mathbf{x})$  used in computing stiffness matrix and material volume depends on the B-spline density  $\tilde{\rho}(\mathbf{x}^d)$  at density evaluation points  $\mathbf{x}^d$ , not on neighboring elements. Therefore, this formulation does not require access of finite element neighborhood information as otherwise would be required in the usual density filter based approach.*

It should be noted that those B-spline coefficients that do not have any influence over the design domain will have zero sensitivity over the cost function and the volume constraint. Therefore, in a gradient based approach, these coefficients do not change during the optimization iterations.

## 4 B-spline as a filter

In previous section, we have given algebraic description of our formulation for topology optimization in B-spline space. Now we proceed to show that in such a formulation, B-splines serve as a filter for topology optimization.

### 4.1 Geometric interpretation: B-spline is a filter with inherent length scale

The B-spline represented density  $\tilde{\rho}$  and the design variables (B-spline coefficients)  $\rho_i$  are related through equation (17) and the sensitivity is shown in equation (18). These two equations are of

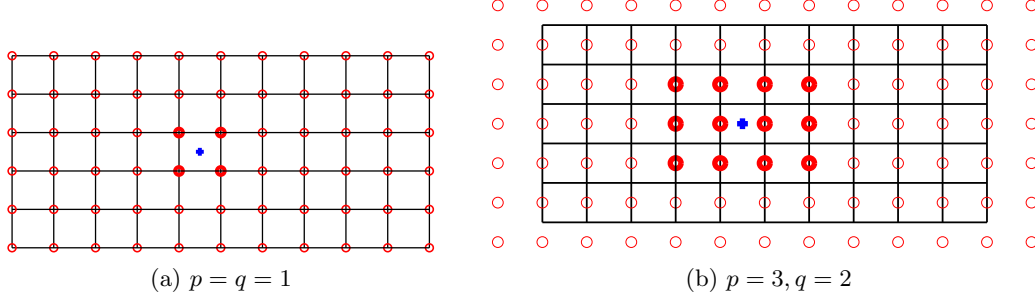


Figure 7: The density (blue point) at each knot span is affected by surrounding  $(p + 1) \times (q + 1)$  B-spline coefficients (shown as bold red circles).

the same form as the usual density filters [11, 10]. The usual density filter can be noted [33] as

$$\tilde{\rho}_i = \frac{\sum_{j \in N_{e,i}} w(\mathbf{x}_j) v_j \rho_j}{\sum_{j \in N_{e,i}} w(\mathbf{x}_j) v_j}, \quad (20)$$

where  $v_j$  represents the volume of element  $j$ ,  $N_{e,j}$  represents the set of neighboring elements lying within the filter domain for element  $i$  and the weighting function is usually defined as a distance based hat function

$$w_h(\mathbf{x}) = \frac{1}{r} \left( 1 - \frac{|\mathbf{x}|}{r} \right). \quad (21)$$

Comparing equations (17) and (20), it is clear that B-spline based density representation can be viewed as a B-spline based filter for design variables  $\rho_i$  in finite element analysis, i.e. the density variables that participate in the finite element analysis is a spatial average of adjacent B-spline coefficients. Figure 7 highlights how a density point  $\tilde{\rho}(\mathbf{x}^d)$  in any given knot span is determined by its adjacent  $(p + 1) \times (q + 1)$  B-spline coefficients.

The difference between the B-spline filter and the usual density filters is three-fold:

- *Weight function.* Here the weighting function is the B-spline shape function (2) that is piecewise polynomials of degree  $p \times q$ , instead of usually a distance based linear hat function (21) that is controlled by the filter radius  $r$ . In the B-spline weight function, the weight value for a density evaluation point  $\mathbf{x}^d$  depends on the location of  $\mathbf{x}^d$  with respect to the knots in the B-spline design representation, not on other density evaluation points or other FE element points. In the usual density filter, the weight value depends on distance between adjacent density variables, usually represented based on finite elements, e.g. element center or element node.
- *Influence region.* Instead of usual axial-symmetric circular filter region as characterized by filter radius in (21), the B-spline filter has a rectangular influence region. For a given B-spline domain  $\bar{\Omega}$  that bounds the design domain  $\Omega$ , when the number of knot intervals increases (i.e. the design resolution increases), each knot interval's length in physical space becomes smaller. As shown in Fig. 3, the weight (shape) function spans  $(p + 1) \times (q + 1)$  knot intervals.
- *Resolution constraint.* Although the analysis density is a filtered representation of B-spline coefficients as shown in (17), this in and of itself is not sufficient to preclude numerical

artifacts such as checkerboard from appearing in optimized design. For a filter to be effective in removing numerical artifacts in topology optimization, the filter function's support needs to span multiple analysis elements. In the usual density filters, the design representation of density distribution is based on the finite element mesh, thus the filter size is explicitly chosen to be larger than the element size for it to be effective. In the B-spline based filter, for the filter to be effective, the support of B-spline basis functions must contain multiple analysis elements, i.e. the resolution of B-spline representation in terms of size of knot intervals  $\delta_x \times \delta_y$  and the analysis representation in terms of element size  $h$  need to be constrained.

Thus, the B-splines, as a filter for topology optimization, are characterized by the degrees of B-splines, the number of knot intervals  $m_x \times m_y$  and the analysis element size  $h$ . A  $p \times q$  B-spline representation has an inherent length scale and the effective length scale is  $(p+1)\delta_x \times (q+1)\delta_y$  respectively in  $x$  and  $y$  directions. With the effective B-spline filter length and through numerical study in Section 5, we have the following necessary condition for the B-spline filter to be effective in preventing numerical artifacts in topology optimization.

**Necessary condition** *When the support of B-spline function  $(p+1)\delta$  is smaller than the element size  $h$ ,*

$$(p+1)\delta \leq h, \quad (22)$$

*the filter is not effective.*

When  $(p+1)\delta \leq h$  (where  $\delta$  is the size of a knot span), the corresponding B-spline coefficients can affect only one analysis element. Thus in this condition the B-spline filter is not effective for topology optimization and checkerboard may occur. This is demonstrated by numerical results in Section 5.

Through numerical study in Section 5, we also propose a sufficient condition, that is

**Sufficient condition** *When the knot span  $\delta$  is larger or equals to the element size  $h$ ,*

$$h \leq \delta, \quad (23)$$

*there are no checkerboard patterns in optimized designs.*

Since each B-spline basis function spans  $(p+1)\delta$ , when  $h \leq \delta$ , each B-spline basis function spans at least  $p+1$  elements. Thus each B-spline coefficient affects at least  $p+1$  adjacent elements. In such cases, our numerical study shows that there are no checkerboards for all degrees ( $p \geq 1$ ) of B-splines. When  $h \in (\delta, (p+1)\delta]$ , whether the B-spline filter is effective in suppressing checkerboards or not depends on the degrees of B-splines and the resolution contrast  $\alpha = h/\delta$  between the element size  $h$  and knot span  $\delta$  assuming square elements and square knot spans. That B-splines is a filter with inherent length scale thus provides a geometric explanation for the next section on why there are no numerical artifacts such as checkerboards and how the minimal length scales of optimized topology are affected by the degrees and knot intervals with B-spline parameterization. See Section 5.1.1 for more details.

## 4.2 Analytical analysis of B-spline representation of density

In this subsection, we present propositions on B-spline representation of density with the goal of illustrating the effect of increasing B-spline degrees and reducing B-spline resolution on density used in analysis. They have the effect of reducing the density difference between adjacent analysis elements. We assume  $\rho_i \in [0, 1]$  as required in the formulation (6).



We now show the transition from a solid knot interval to zero density knot interval in 1D.

**Proposition 1** *If any point  $x_a$  interior to a knot span  $(\bar{x}_j, \bar{x}_{j+1})$  has density 1, then the density in the entire knot range  $(\bar{x}_{j-p}, \bar{x}_{j+p+1})$  is non-zero. That is, if*

$$\exists x_a \in (\bar{x}_j, \bar{x}_{j+1}), \quad \tilde{\rho}(x_a) = 1,$$

*then*

$$\forall x \in (\bar{x}_{j-p}, \bar{x}_{j+p+1}), \quad \tilde{\rho}(x) > 0.$$

**Proof.** By definition of B-splines, we have  $\tilde{\rho}(x_a) = \sum_{i=j-p}^j B_{i,p}(x_a)\rho_i$ . Since  $\rho_i \in [0, 1]$  and  $B_{i,p}(x) \in [0, 1]$ , we have  $\sum_{i=j-p}^j B_{i,p}(x_a)\rho_i \leq \sum_{i=j-p}^j B_{i,p}(x_a) = 1$ . A basis function  $B_{i,p}$  spans the knot intervals  $[\bar{x}_i, \bar{x}_{i+p+1}]$  and is 0 only at  $x = \bar{x}_i$  or  $\bar{x} = \bar{x}_{i+p+1}$ . If  $\tilde{\rho}(x_a) = 1$  thus its  $p+1$  coefficients must all be 1, i.e  $\rho_i = 1, i = j-p, \dots, j$ . We thus have that the density  $\tilde{\rho}$  is non-zero between  $2p+1$  knot intervals  $(\bar{x}_{j-p}, \bar{x}_{j+p+1})$ . ■

This proposition shows that for a degree  $p$  B-spline, if there is one solid point in the interior of a knot interval  $(\bar{x}_j, \bar{x}_{j+1})$ ,  $p$  knot intervals smaller than  $\bar{x}_j$  and  $p$  knot intervals larger than  $\bar{x}_{j+1}$  all have non-zero density. It can also be inferred from the proof that, if a solid point is interior to a knot interval, then the density in the entire knot interval is solid. It can be further seen that the above proposition can also be extended to the transition from void knot interval to grayscale density knot intervals as follows.

**Corollary 2** *If any point  $x_a$  that is interior to a knot span  $(\bar{x}_j, \bar{x}_{j+1})$  has density 0, then the density in the entire knot range  $(\bar{x}_{j-p}, \bar{x}_{j+p+1})$  is smaller than 1. That is, if*

$$\exists x_a \in (\bar{x}_j, \bar{x}_{j+1}), \quad \tilde{\rho}(x_a) = 0,$$

*then*

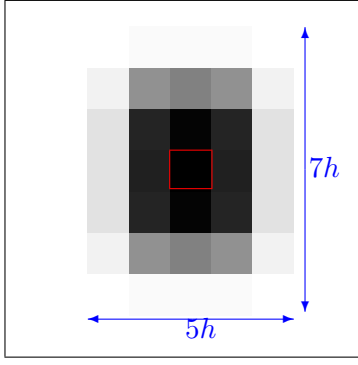
$$\forall x \in (\bar{x}_{j-p}, \bar{x}_{j+p+1}), \quad \tilde{\rho}(x) < 1.$$

Due to the tensor product nature of B-spline representation, we have the following corollary.

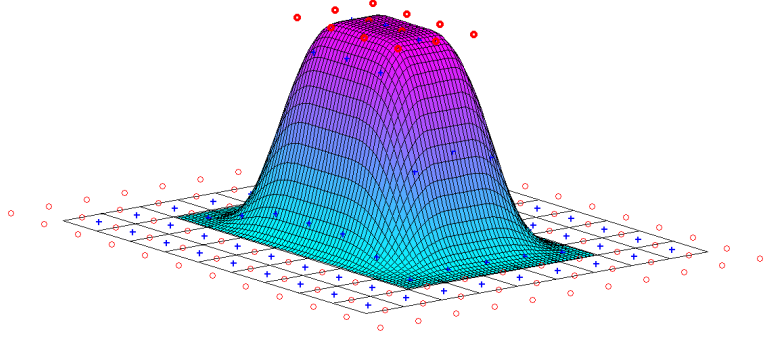
**Corollary 3** *The gray transition from solid to void or from void to solid spans  $p$  knot intervals in  $x$  direction and  $q$  knot intervals in  $y$  direction.*

Figure 8 gives an illustration of gray transition from a solid element to void elements. The underling design representation is a  $p = 2, q = 3$  B-spline with  $9 \times 9$  knot intervals. To represent a solid analysis element,  $3 \times 4$  B-spline coefficients of value 1 are used and all other coefficients are 0 (shown as red circles in Fig. 8b). It is clear from Fig. 8a that with such a solid element, the neighboring 2 elements on both sides of  $x$  direction and neighboring 3 elements on both sides along  $y$  directions all have non-zero densities. That is, the gray transition spans on each side  $p$  knot intervals in  $x$  direction and  $q$  knot intervals in  $y$  direction.

A checkerboard consists of alternation of void and solid, i.e. densities  $\bar{\rho}_i = 0$  or 1, in adjacent elements. The appearance of checkerboard can be ascribed to the fact that alternating void/solid density in adjacent elements leads to artificial stiffness in linear quadrilateral element based analysis [3], thus the optimizer would produce such checkerboard for maximal stiffness. Here we conjecture that restricting the allowed maximal density difference in adjacent elements in the design space is useful for suppressing checkerboard. We show that the B-spline filter effectively restricts the allowed density difference between adjacent elements.



(a) 2D view of piecewise density distribution  $\tilde{\rho}$  with the center element as solid.



(b) 3D view of continuous density  $\tilde{\rho}$  and B-spline coefficients  $\rho$ .

Figure 8: Gray transition spanning  $p$  or  $q$  knot intervals on each side: a degree  $p = 2, q = 3$  B-spline of  $9 \times 9$  knot intervals is used to represent a solid element at the center. The solid center element is highlighted in (a) and the transitions span 5 elements in x direction and 7 elements in y direction. A 3D visualization of continuous density  $\tilde{\rho}$  is shown in (b). Red circles represents the B-spline coefficients and blue cross represents where  $\tilde{\rho}$  for each analysis element is sampled. Black grid represents the quadrilateral elements.

For any two points  $x_a$  and  $x_b$ , their density can be expressed as  $\tilde{\rho}(x_a) = \sum_{i \in I_a} \rho_i N_i(x_a)$  and  $\tilde{\rho}(x_b) = \sum_{j \in I_b} \rho_j N_j(x_b)$  where  $I_a$  and  $I_b$  respectively represent  $p+1$  number of indicies for B-spline coefficients  $\rho_i$  and  $\rho_j$  that have influence at  $x_a$  and  $x_b$ . The difference in their density  $\tilde{\rho}(x_a) - \tilde{\rho}(x_b)$  can be expressed as

$$\tilde{\rho}(x_a) - \tilde{\rho}(x_b) = \sum_{i \in I_a} \rho_i N_i(x_a) - \sum_{j \in I_b} \rho_j N_j(x_b) \quad (24a)$$

$$= \sum_{i \in I_a \setminus I_{ab}} \rho_i N_i(x_a) - \sum_{j \in I_b \setminus I_{ab}} \rho_j N_j(x_b) + \sum_{k \in I_{ab}} \rho_k (N_k(x_a) - N_k(x_b)) \quad (24b)$$

where  $I_{ab} = I_a \cap I_b$  is the intersection of index sets  $I_a$  and  $I_b$ . We thus have the following proposition.

**Proposition 4** *The maximal density difference between two points  $x_a$  and  $x_b$  depends on the basis functions that have non-zero influence over both points. More specifically,*

$$\max(\tilde{\rho}(x_a) - \tilde{\rho}(x_b)) = 1 - \sum_{k \in I_{ab}} \min(N_k(x_a), N_k(x_b)), \quad (25)$$

where  $I_{ab} = I_a \cap I_b$ .

**Proof.** In order to maximize the density difference  $\tilde{\rho}(x_a) - \tilde{\rho}(x_b)$  between two points  $x_a$  and  $x_b$ , since all basis functions are non-negative, we have  $\rho_i = 1$  and  $\rho_j = 0$  from (24a). So from (24b) we have

$$\max(\tilde{\rho}(x_a) - \tilde{\rho}(x_b)) = \max \left( \sum_{i \in I_a \setminus I_{ab}} N_i(x_a) + \sum_{k \in I_{ab}} \rho_k (N_k(x_a) - N_k(x_b)) \right). \quad (26)$$

The values of  $\rho_k$  depends on the sign of  $N_k(x_a) - N_k(x_b)$ . If  $N_k(x_a) - N_k(x_b) \geq 0$ ,  $\rho_k = 1$ . Otherwise,  $\rho_k = 0$ . So we further split the set  $I_{ab}$  into two sets:  $I_{ab}^+$  corresponding to  $N_k(x_a) - N_k(x_b) \geq 0$  and  $I_{ab}^-$  corresponding to  $N_k(x_a) - N_k(x_b) < 0$ . The equation (26) can then be simplified as

$$\begin{aligned}
\max(\tilde{\rho}(x_a) - \tilde{\rho}(x_b)) &= \sum_{i \in I_a \setminus I_{ab}} N_i(x_a) + \sum_{k \in I_{ab}^+} (N_k(x_a) - N_k(x_b)) \\
&= \sum_{i \in I_a \setminus I_{ab}} N_i(x_a) + \sum_{k \in I_{ab}^+} N_k(x_a) + \sum_{k \in I_{ab}^-} N_k(x_a) - \sum_{k \in I_{ab}^-} N_k(x_a) - \sum_{k \in I_{ab}^+} N_k(x_b) \\
&= \sum_{i \in I_a} N_i(x_a) - \sum_{k \in I_{ab}^-} N_k(x_a) - \sum_{k \in I_{ab}^+} N_k(x_b) \\
&= 1 - \sum_{k \in I_{ab}^-} N_k(x_a) - \sum_{k \in I_{ab}^+} N_k(x_b).
\end{aligned} \tag{27}$$

In the last part, we used the partition of unity property of B-spline basis functions. The last part in the equation above equals to  $1 - \sum_{k \in I_{ab}} \min(N_k(x_a), N_k(x_b))$  after we combine the index sets  $I_{ab}^-$

and  $I_{ab}^+$ . ■

This proposition shows that, when two points have a larger number of overlapping basis functions (i.e. larger  $I_{ab}$ ) or larger overlapping basis function values (i.e. larger  $\min(N_k(x_a), N_k(x_b))$ ), the density difference allowed by the B-spline representation becomes smaller. In practice, when we increase the degrees of B-spline functions or reduce the number of knot spans for a given B-spline domain, we effectively restrict the allowed density difference between any two adjacent elements.

## 5 Topology optimization in rectangular design domains

In this section, we present numerical results of topology optimization in B-spline space where the design domain is of rectangular shape. The optimization results of curved design domains are shown in the next section. Here we focus on the role of the B-spline based density representation in suppressing numerical artifacts and controlling minimal feature length in optimized structures. We also show the use of B-spline representation for multi-resolution designs. Numerical experiments have been conducted on the minimal compliance, compliant mechanism and heat conduction problems. All analysis in this section is done with quadrilateral four-node (Q4) linear elements and the density variables in each element is element-wise constant.

An illustration of the three test problems, MBB beam, compliant inverter, and heat conduction, with design domains and boundary conditions are shown in Figure 9. For the MBB example, the objective is to minimize the compliance where the Young's modulus  $E_0 = 1$  and  $E_{\min} = 1.0e - 9$ , and the volume fraction  $\gamma = 0.5$ . The design domain and the boundary conditions for the inverter and heat conduction are the same as those in [33]. For the compliant inverter, we use (9) to represent the density power law where  $E_0 = 1$  and  $E_{\min} = 1.0e - 9$ . The objective is to maximize the negative output displacement  $u_{\text{out}}$ . The spring stiffness  $k_{\text{in}} = 1$  and  $k_{\text{out}} = 0.001$ , and the force vector  $f_{\text{in}} = 1$ . The volume fraction is 0.3. For the heat conduction, the design objective is to maximize the transfer of the heat  $\mathbf{f}^T \mathbf{u}$  generated in the design domain where it is under a unit distributed thermal load. The conductivities for the solid and the void phases are  $E_0 = 1$  and  $E_{\min} = 0.001$ . The volume fraction is 0.5.

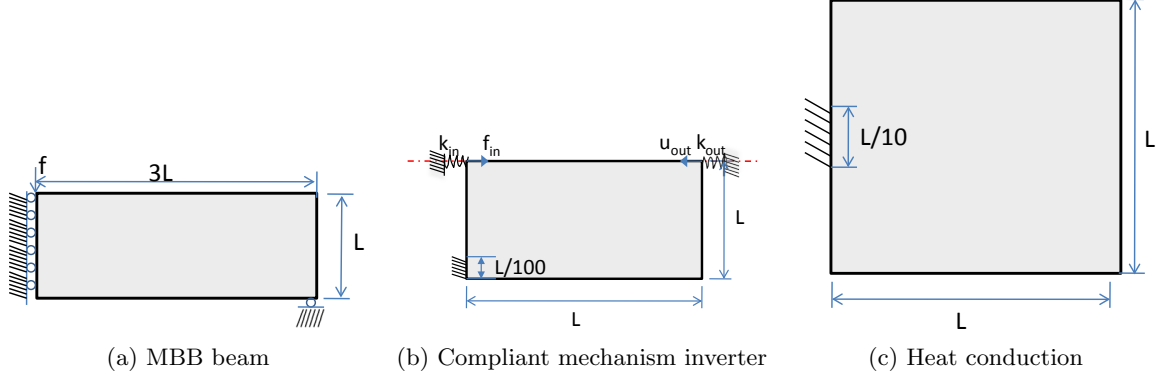


Figure 9: Design domain and boundary conditions for (a) MBB beam, (b) compliant inverter, and (c) heat conduction.

In the examples in this paper, the B-spline degrees  $p$  in  $x$  and  $q$  in  $y$  directions are the same, unless otherwise noted. The optimization is done by the Method of Moving Asymptotes [34] with the termination criteria being that the maximum change of design variables  $\rho_i$  is 0.01 and the maximum allowed iteration number is 500. The penalty coefficient  $s$  in the power law is 3 in all cases. The penalty is increased at the increment of 0.04 per iteration until it reaches 3. The initial designs are all of uniform density and satisfy the volume fraction constraints, unless they are in successive optimization. In successive optimization, the optimized designs at a coarse resolution are set as initial designs for optimization at a finer resolution. For convenience of comparison with optimized results from the existing density filter, all optimized designs plotted in this section are the piecewise constant density  $\bar{\rho}$  in each analysis element unless otherwise specified.

## 5.1 Minimal compliance in MBB beam

### 5.1.1 Numerical artifacts and filtering

In this subsection, we use numerical study to show that B-spline is effective in preventing checkerboard in optimized designs. As shown earlier, the B-spline filter for topology optimization is determined by the B-spline degree, the number of knot spans (design resolution) and the number of analysis elements (analysis resolution). We here use MBB example where the analysis is done with  $n_x \times n_y = 96 \times 32$  Q4 linear elements and the density distribution is represented by B-splines of different degree  $p = q$  and different knot spans  $m_x \times m_y$ . Both elements and knot spans are square, thus resolution contrast  $\alpha = h/\delta = m_y/n_y = m_x/n_x$ .

The influence size of B-spline coefficients is  $(p+1)\delta$  where  $\delta$  represents the knot span. Therefore, either reducing the number of knot spans for a given B-spline domain or the increase of B-spline degree effectively increases the B-spline filter size. Figure 10 shows that reducing the number of B-spline knot spans is effective in removing checkerboard. In this figure, the designs are obtained with quadratic B-splines of different number of knot spans, but analyzed with the same number of elements. In the paper, we use a prefix ‘‘A’’ and ‘‘D’’ before a pair of numbers to represent the number of analysis elements and the number of B-spline knot spans. The cost function values and optimization iteration number are shown in the figure with prefix ‘c’ and ‘I’. When the number

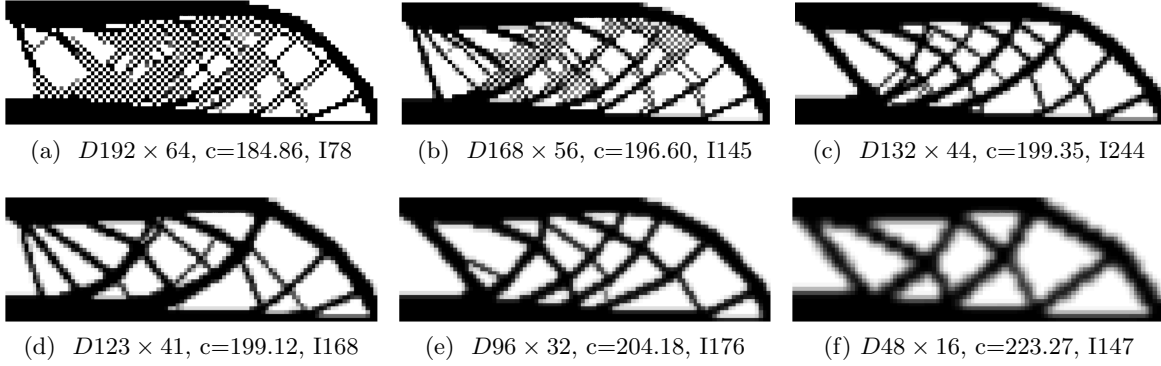


Figure 10: Reducing the number of B-spline knot spans is effective in removing checkerboard. All B-splines in this figure are quadratic  $p = 2$ . The analysis is done by  $96 \times 32$  linear elements.

of knot spans  $m_y$  equals to 64 or 56, there are checkerboard in the optimized designs. As the number of B-spline knot spans decreases, i.e. the ratio of design resolution with respect to analysis resolution of density representation  $\alpha$  decreases, the corresponding cost function increases and the minimal feature size increases. When the number of knot span in  $y$  direction is 41 (Fig. 10d), the checkerboard disappears. That is, when the number of knot span decreases while the number of analysis elements kept the same, the effective filter size increases, leading to the suppression of checkerboard. Figure 11 shows that the increase of the B-spline degrees can also be used to suppress checkerboard. This is because, with the same design resolution, i.e. knot spans are the same, as the degree increases, the B-spline's effective filter size grows. As both Fig. 10 and Fig. 11 show, as an overall trend, the design is generally less and less complex as the design resolution becomes coarse and the degree of the basis increases. Individual designs from degree to degree may vary slightly in complexity as shown in cases  $p = 5$  and  $p = 6$  in Fig. 11. In Fig. 11, the optimization was terminated after 500 iterations. If the iterations continues, it takes 918 iterations to converge with compliance of 197.0215 at  $p = 7$  and it takes 773 iterations to converge with compliance of 198.4451 at  $p = 9$ . There is no difference from optimized topology terminated at 500 iterations.

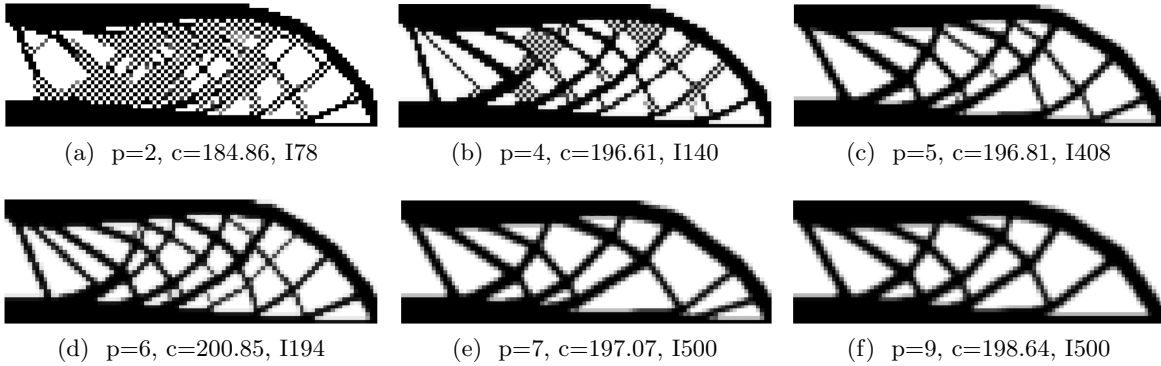


Figure 11: Increasing B-spline degrees can suppress checkerboard. The analysis is done by  $96 \times 32$  linear elements and the density distribution is represented by  $D192 \times 64$ .

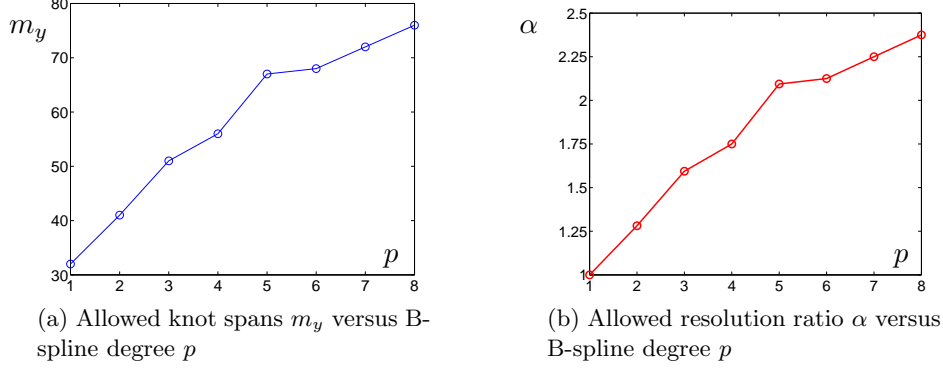


Figure 12: The increase of B-spline degrees allows increased design resolution (i.e. more B-spline knot spans) without causing checkerboards.

Since either reducing the B-spline resolution (number of knot spans) or increasing the B-spline degree can increase the filter size and suppress checkerboard, one can combine them both to see what is the allowed maximum number of knot spans (i.e. highest design resolution), for a given B-spline degree and given number of analysis elements, without causing checkerboard. Figure 12a shows for MBB beam the allowed knot spans  $3m_y \times m_y$  for B-spline degrees  $p = 1$  to 8. For linear degree, the largest number of knot spans without causing checkerboard is just 32, same as the number of analysis elements. For  $p = 2$ , the number is 41, as shown in Fig. 10d. As the degree  $p$  increases, the allowed knot spans increases. Figure 12b shows the normalized ratio of allowed design resolution versus analysis resolution  $\alpha = \frac{m_y}{n_y} = \frac{m_x}{n_x}$  with respect to the B-spline degree.

The key observation is that, as the B-spline degree increase, the allowed design resolution (number of knot spans) can also increase. The allowed design resolution can be larger than the analysis resolution (number of analysis elements) when degree  $p$  is larger than 1. Therefore, for a given element size  $h$ , one can choose knot span size  $\delta$  and degree  $p$  so that the point  $(p, \alpha) = (p, h/\delta)$  is below the curve in Fig. 12b in order to avoid checkerboard.

For better illustration of our B-spline based density representation, we also plot the B-spline represented continuous density representation. Figure 13 plots the B-spline coefficients (1st column), the corresponding B-spline represented continuous density  $\tilde{\rho}(\mathbf{x})$  (2nd column) and the piecewise constant density representation  $\bar{\rho}(\mathbf{x})$  used in analysis (third column) for designs resulting from degrees  $p = 4$  and  $p = 9$ . These designs correspond to the designs Fig. 11b and Fig. 11f.

### 5.1.2 Filter size and minimal feature length

Having demonstrated how the number of knot spans and degrees can be used to suppress checkerboards, we now proceed to show how these factors can be used to control minimal feature length in optimized designs and we also compare the results with those from the usual density filter. Figure 14 shows how reducing the number of knot spans increases the minimal feature length. In this figure, all designs are analyzed with  $90 \times 30$  analysis elements and parameterized with cubic  $p = 3$  B-splines. As the number of knot spans reduces from  $135 \times 45$  (Fig. 14a) to  $27 \times 9$  (Fig. 14i), the topology becomes simpler and the minimal feature length becomes larger. The cost function generally increases as the number of knot spans decreases, although the cost function for  $D105 \times 35$  is slightly smaller than that of  $D120 \times 40$ .

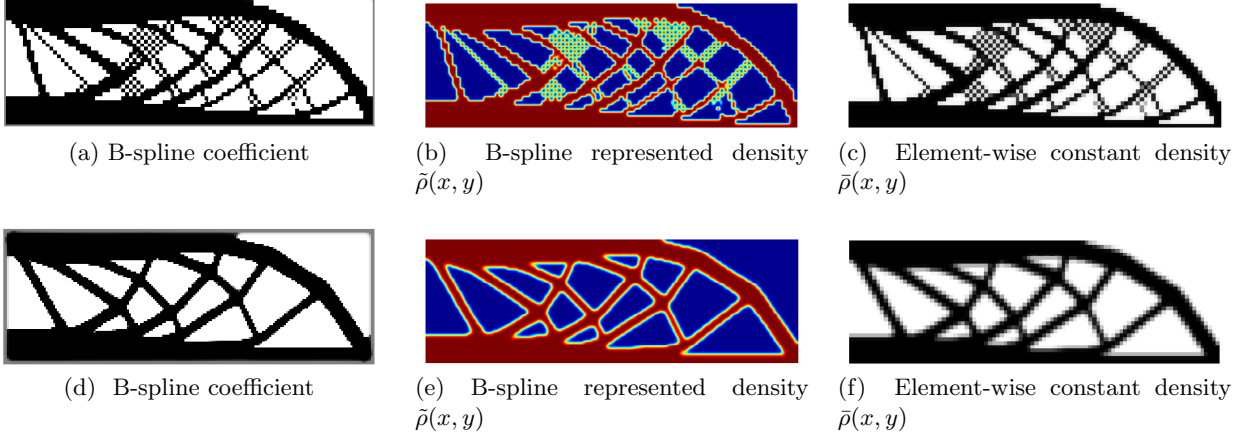


Figure 13: Density display. B-spline coefficients (1st column), B-spline represented continuous density  $\tilde{\rho}(x,y)$  (2nd column) and the corresponding element-wise constant density  $\bar{\rho}(x,y)$  used in analysis (third column). Top row:  $p = 4$  and bottom row:  $p = 9$ .

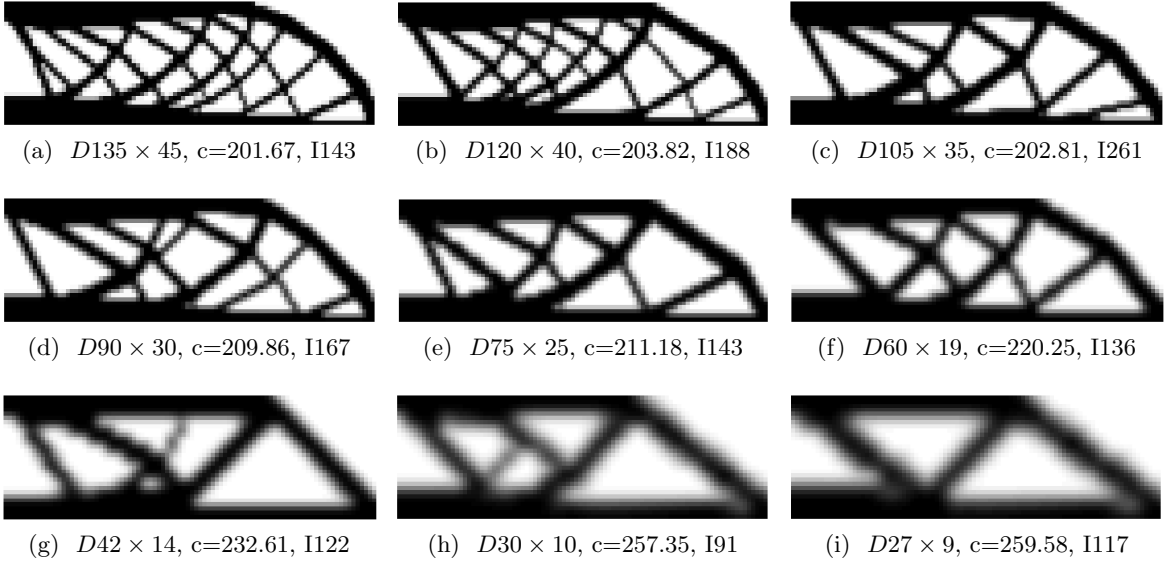


Figure 14: Reducing the number of B-spline knot spans leads to larger minimal features. B-spline degree  $p = 3$  with analysis element resolution  $A90 \times 30$ .

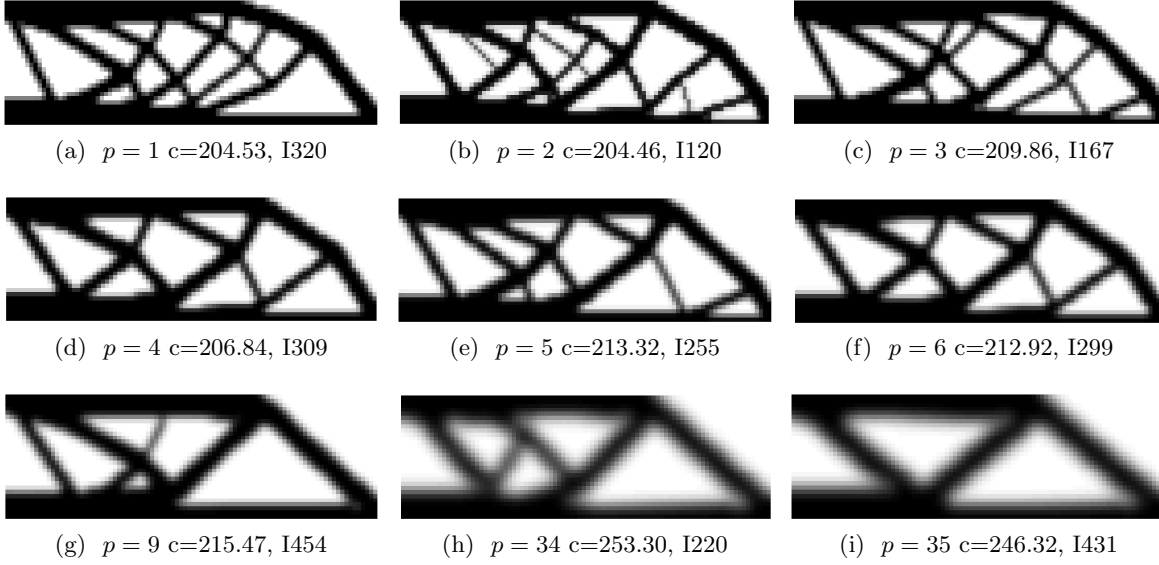


Figure 15: Increasing B-spline degrees leads to increased feature size. The analysis resolution is  $A90 \times 30$  and the design resolution is  $D90 \times 30$ .

Figure 15 shows that increasing B-spline degree leads to increased feature size where the analysis resolution is  $A90 \times 30$  and the design resolution is  $D90 \times 30$ . As the degree  $p$  increases, the structural boundary becomes less crisp and more gray elements with density between 0 and 1 occurs along the boundary. These observations are expected per Corollary 3: as the degree  $p$  controls the size of each design variable  $\rho_i$ 's influence region, i.e.  $p$  number of gray knot intervals. Higher degrees  $p$  implies a larger minimal feature and a larger intermediate area transitioning the density from solid to void or from void to solid. With the increase of B-spline degree  $p$ , the obtained compliance in the optimized design also becomes larger.

In order to compare the B-spline based optimization results with those from the density filter based approach, we show a set of optimized designs that are obtained with  $90 \times 30$  linear elements with piecewise constant density parameterization under density filtering (21). Figure 16 shows such a set of optimized MBB beams where the density filter is used to remove the checkerboard patterns. These designs are obtained with the filter radius increasing from 1.1 to 4.2. The topologies obtained with filter radius between 1.7 to 2.8, and between 2.9 and 4.1, are respectively the same. As the figure shows, when the filter radius  $r$  increases, the minimal length of the optimized structures increases accordingly. By comparing the designs in Fig. 16 with those in Fig. 14 and Fig. 15, one can see that the topologies from B-splines with resolution smaller than analysis element resolution (in Fig. 14e) and degree  $p \geq 6$  (in Fig. 15f) are similar to those  $r \geq 1.7$  in Figure 16. The designs obtained with lower degree B-splines ( $p < 6$ ) in ( Fig. 15) and higher resolution (in Fig. 14) and the designs with piecewise constant density parameterization under small filter radius ( $r < 1.7$ ) differ. This difference can be ascribed to the existence of multiple local minimal solutions. This comparison suggests that topology optimization in B-spline space leads to similar optimized design as existing density filter based approach.



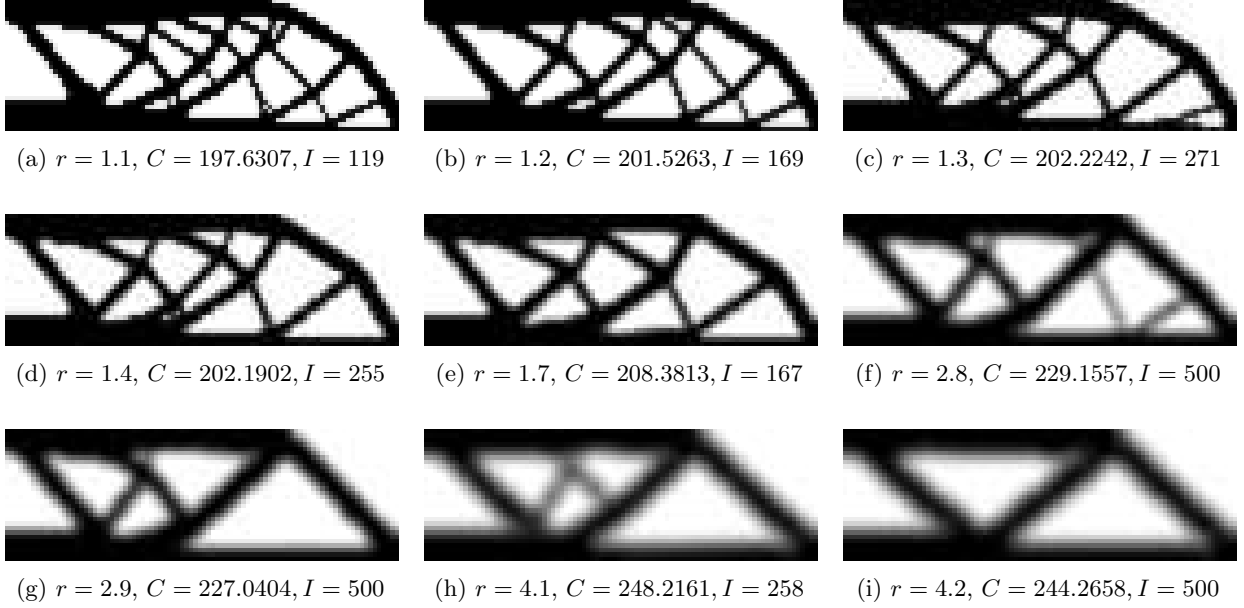


Figure 16: MBB beams optimized with the usual density filter and piecewise constant density parameterization with  $90 \times 30$  linear elements. As the filter radius  $r$  increases, the minimal length of optimized structures increases.

### 5.1.3 Multi-resolution topology optimization by successive refinement of design representation

The use of B-splines to represent the density field make it conducive for multi-resolution topology optimization. That is, one uses coarse resolutions of B-spline density representation to quickly explore and compare different designs and, among these designs, then choose a better design and refine it into finer resolution for further optimization at the finer resolution. Table 1 gives a set of successive optimized design where optimized designs obtained at low design resolutions (i.e. with low number of knot intervals) in the first column are fed as initial designs for optimization at high design resolutions (i.e. double the knot intervals for each refinement) in the second and third column. It is worth noting that in all cases, mesh independence is achieved with respect to design resolutions (i.e. the number of knot intervals) with such successive optimization. Here the mesh independence is achieved due to the use of optimized design from low resolutions as initial designs and the fact the low resolution design space is a subspace of high resolution design space. Thus an optimal design in low resolution design space is also an optimal design in high resolution design space.

Comparing results of the successive optimization from low design resolutions to high design resolutions with results from direct optimization at high design resolutions shown in Fig. 17, the successive optimization leads to optimized design with smaller compliance values and fewer iterations. For example, the design in Table 1 (f) has compliance 193.46 with 314 iterations, while the design (b) in Fig. 17 has compliance 196.19 with 464 iterations. Another difference is that the successive optimization from low design resolutions to high design resolutions leads to

Table 1: Successive optimization from low to high design resolutions by B-splines of different degrees.







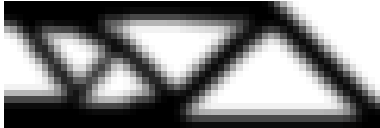
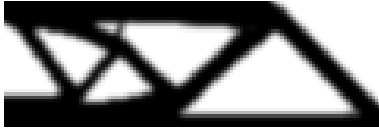




	Initial design resolution	Refinement once	Refinement twice
$p = 1$	(a) $60 \times 20, C = 215.121, I = 151$ 	(b) $120 \times 40, C = 196.519, I = 141$ 	(c) $240 \times 80, C = 189.902, I = 451$ 
$p = 3$	(d) $45 \times 15, C = 227.121, I = 142$ 	(e) $90 \times 30, C = 202.714, I = 96$ 	(f) $180 \times 60, C = 193.455, I = 314$ 
$p = 10$	(g) $60 \times 20, C = 237.878, I = 274$ 	(h) $120 \times 40, C = 207.755, I = 199$ 	(i) $240 \times 80, C = 197.098, I = 340$ 
<hr/>			
			
	(a) $240 \times 80, p = 1, c = 191.91, I500$	(b) $180 \times 60, p = 3, c = 196.19, I464$	(c) $240 \times 80, p = 10, c = 199.65, I500$

Figure 17: Direct optimization at high design resolutions corresponding to the third column in Table 1. The number of analysis elements are respectively same as the number of knot spans in each subfigure.













relatively larger minimal feature length in optimized structures when compared with those from direct optimization at high design resolution. Further, such successive optimization has the effect of making the blur boundary in the designs obtained at low design resolution (1st column) more crisp (as shown in the third column). This is because, with the increased knot intervals, the physical size of each knot interval becomes smaller and thus the gray transition region becomes smaller accordingly.

## 5.2 Compliant mechanism

We have also extended the B-spline based topology optimization to the design of compliant inverter. Table 2 compares a set of designs obtained with B-splines of degree 1, 3, 5, and 10 under different optimization schemes. In all cases, the numbers of Q4 linear analysis elements are the same as the respective numbers of knot spans. The first column shows the designs optimized at low design resolution ( $100 \times 50$  knot spans). The second column shows the designs optimized successively with

design representation refinement where the designs from low resolution in the first column are used as initial designs for design at higher resolution ( $200 \times 100$  knot spans). It is clear that respectively the same topologies are obtained as the initial designs in the first column, but with larger inverting force and clearer structural boundary. The third column shows the designs directly optimized at higher design resolution, which leads to smaller features in optimized structures and larger inverting force than the designs obtained with coarse resolution (in the 1st column). This is because higher design resolution corresponds to smaller effective filter size (thus smaller features) and larger design space (thus better inverting force). Comparing the second and third columns where the designs are obtained under the same number of design resolutions and the same number of analysis elements, the designs with successive refinement of design representation contain larger features, with nearly the same or even slightly better inverting forces. This example shows that B-spline based multi-resolution designs allows the use of coarse resolution for more efficient exploration of different initial designs. Comparing the designs obtained in different rows, one can see that, as the B-spline degrees increase from  $p = 1$  to  $p = 10$ , the minimal feature length in the optimized designs also becomes larger. This suggests that again the B-spline degree can be used to control the minimal feature length.

Table 2: Optimized inverters by B-splines of different degrees under various optimization schemes.

	100×50	200×100 (successive )	200×100 (direct )
$p = 1$	(a) $C = -2.347, I = 363$ 	(b) $C = -2.472, I = 451$ 	(c) $C = -2.444, I = 500$ 
$p = 3$	(d) $C = -2.3297, I = 346$ 	(e) $C = -2.4497, I = 202$ 	(f) $C = -2.4570, I = 500$ 
$p = 5$	(g) $C = -2.3094, I = 500$ 	(h) $C = -2.4493, I = 372$ 	(i) $C = -2.4136, I = 500$ 
$p = 10$	(j) $C = -2.1906, I = 222$ 	(k) $C = -2.3932, I = 500$ 	(l) $C = -2.3805, I = 437$ 

### 5.3 Heat conduction

The heat conduction problem is known to involve checkerboard challenges. We show below a set of experiments that illustrate the influence of B-spline degrees and the effect of multi-resolution designs.

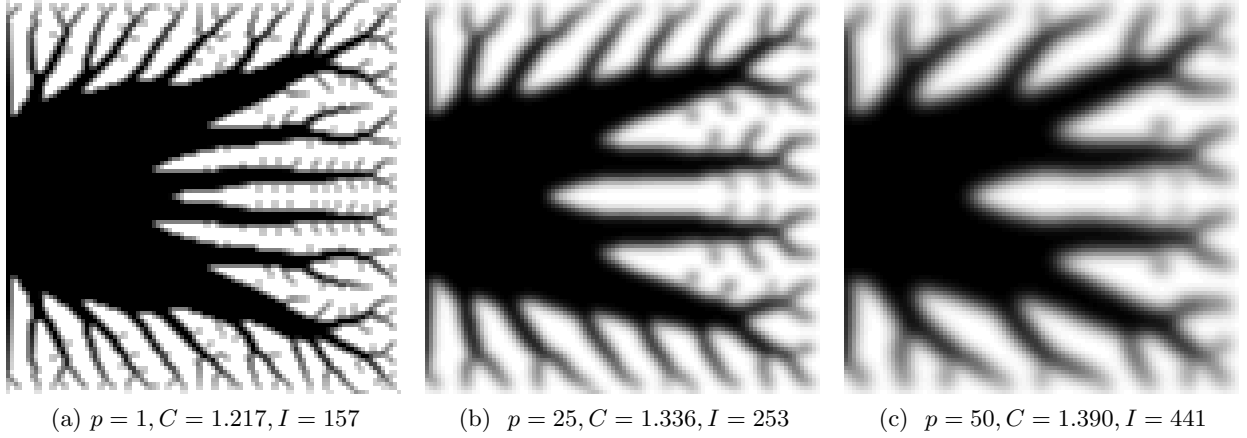


Figure 18: Optimization of heat conduction via B-splines of different degrees. They all have  $100 \times 100$  knot spans and analyzed with  $100 \times 100$  Q4 linear elements.

Figure 18 shows the results of optimization of heat conduction represented by B-splines of different degrees. They all have  $100 \times 100$  knot spans and analyzed with  $100 \times 100$  Q4 linear elements. They are the optimized designs with B-splines of degree 1, 25, and 50. Comparing these designs, one can see that higher degrees of B-splines filters out smaller features in the optimized structures and the resulting designs have larger objective function values.

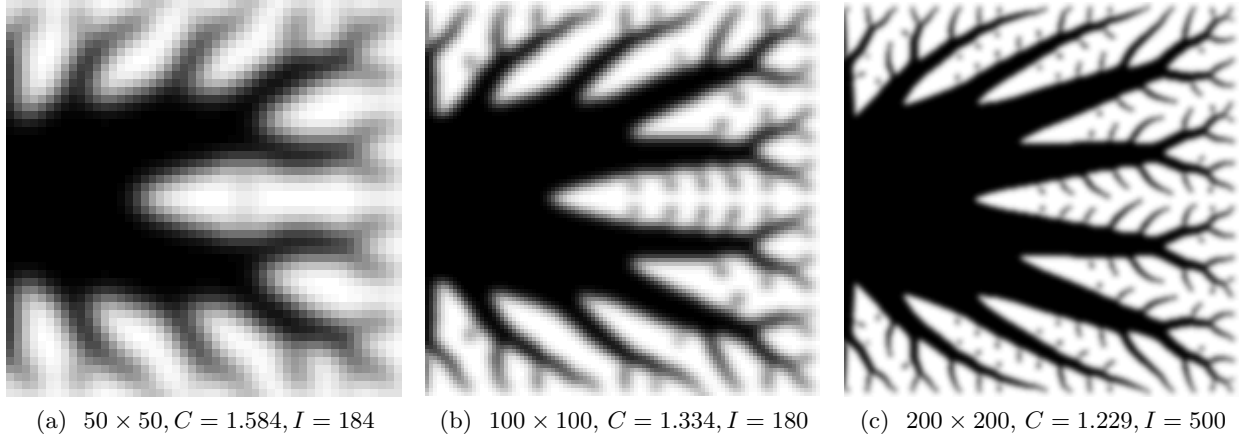


Figure 19: Successive optimization via refinement of design representation. The B-spline is of degree  $p = 25$ . (a) optimized design from  $50 \times 50$  knot intervals, (b) optimized design with initial design from (a) and the design resolution refined into  $100 \times 100$  knot intervals, (c) optimized design with the initial design from (a) and the design resolution refined into  $200 \times 200$  knot intervals.

Figure 19 shows successive optimization via refinement of design representation: (a) optimized design from  $50 \times 50$  knot spans, (b) optimized design with initial design from (a) and optimized at design resolution  $100 \times 100$  knot spans, (c) optimized design with design resolution  $200 \times 200$  knot spans. The B-spline is of degree  $p = 25$ . The analysis mesh resolutions are respectively the same as B-spline resolutions (knot spans). This example shows that the successive optimization via refinement of design representations (i.e. knot spans) preserves the overall topology as in the coarse mesh from the initial design, and makes the gray structures in low design resolution clearer and sharper.

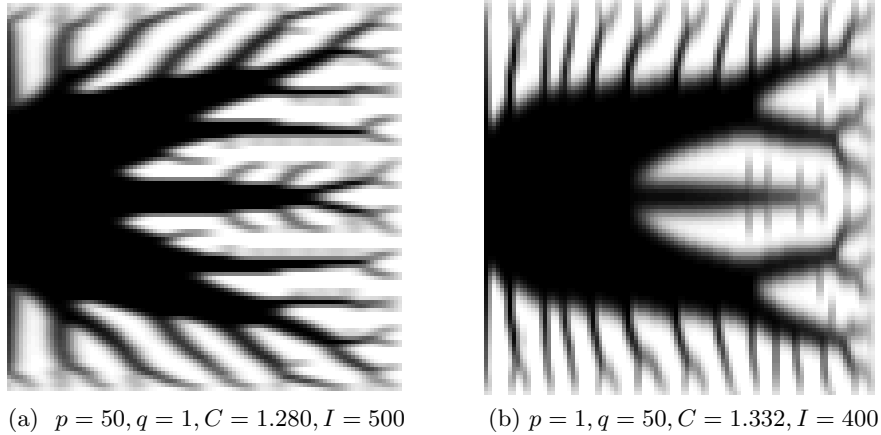


Figure 20: Influence of unequal B-splines degrees in heat conduction optimization. They have  $100 \times 100$  knot intervals and analyzed with  $100 \times 100$  Q4 linear elements.

Figure 20 gives an illustration of anisotropic control of feature length in heat conduction optimization via unequal B-spline degrees. Figure 20a shows the optimized design with the B-spline degrees of  $p = 50$  in  $x$  and  $q = 1$  in  $y$  directions. Figure 20b shows the B-splines of degree  $p = 1$  in  $x$  and  $q = 50$  in  $y$  directions. Comparing the two designs, it is clear that higher B-spline degree in one direction and low degree in the other direction leads to long features in the higher-degree direction and thin features in lower-degree direction. For this particular heat conduction problem, since the heat sink is on the left side, higher degrees on the  $x$  direction apparently leads to lower objective function values.

## 6 Topology optimization of curved domains

In the previous section, we have demonstrated various numerical results of topology optimization in B-spline space for problems with rectangular domains where piece-wise constant material density is used in a linear quadrilateral element based FE analysis. In this section, we aim to show that the proposed approach works equally well for problems of curved domains and can be analyzed with other forms of analysis elements such as linear triangular elements based FE analysis and NURBS based isogeometric analysis. To demonstrate the versatility of our approach regarding how B-spline represented density can be used in analysis, in linear triangular elements, the density for analysis is evaluated at each node point. In NURBS elements, the density for analysis is evaluated at each quadrature point. The triangular elements based FE is implemented via a commercial

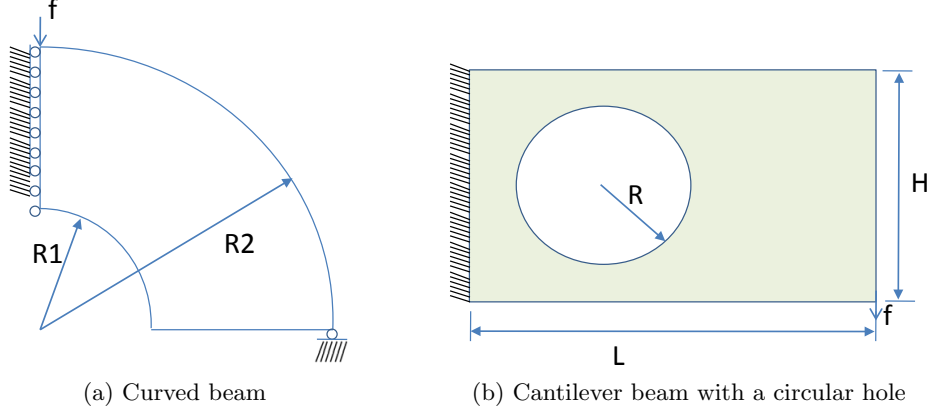


Figure 21: Curved design domains for topology optimization.

FE software COMSOL and the NURBS based analysis was implemented based on own in-house software [28, 35].

Figure 21 shows two curved design domains for compliance minimization. In both cases,  $E = 1$  and  $E_{\min} = 1.0e^{-9}$  and Poisson's ratio is 0.3. Figure 21a shows a circular beam and the load is on the top-left corner with  $R1 = 1$  and  $R2 = 3$ . Figure 21b shows a cantilever beam with a circular hole, where the left side is fixed and the beam is under vertical load at the low-right corner. In this domain,  $L = 9$ ,  $H = 6$ ,  $R = 2$  and the center of the hole with respect to low-left corner is 1.5 in both horizontal and vertical distance. This problem has been studied in [36, 37].

### 6.1 B-spline based topology optimization with triangular linear elements

The discretization of the design domains via triangular elements and the embedding of the mesh nodes into the B-spline domains are respectively shown in Fig. 6a, b, and Fig. 22. The left column shows the two design domains are discretized into triangular elements with maximum element size respectively as  $h = 0.15$  and  $h = 0.25$ . The right column shows the nodes in the respective domains of bi-quadratic ( $p = q = 2$ ) B-splines. There are respectively  $m_x \times m_y = 20 \times 20$  and  $m_x \times m_y = 30 \times 20$  knot spans. There are  $p + 1$  extra knots at each end of knot axes.

Figure 23 shows the optimized results of the curved beam (corresponding to Fig. 21a) with linear triangular elements. Figure 23a shows that there is checkerboard like numerical artifact in the optimized design when the optimization is done with the maximum element size  $h = 0.05$ , density parameterized by bi-quadratic B-splines of  $150 \times 150$  knot spans. The compliance is 50.11. When the B-spline degree is increased to 6 and correspondingly the influence region of each B-spline coefficient has increased, the resulting design is free from checkerboard (Fig. 23b). When the mesh density is increased to  $h = 0.03$ , with degree 6 B-splines of the same number of knot spans ( $150 \times 150$ ) as in Fig. 23a, the optimized design (Fig. 23c) has slightly more complex topology. The compliances in Fig. 23b and Fig. 23c are respectively 50.14 and 51.54. When the design in Fig. 23b is analyzed with mesh size  $h = 0.03$ , the compliance is 52.54. This example illustrates that the increase of B-spline degree leads to optimized design free from checkerboard.

Figure 24 shows the role of B-spline filters in optimization of the cantilever beam with a circular hole via triangular elements with the maximum element size  $h = 0.06$ . From Fig. 24a to Fig. 24e, the density distributions are parameterized with  $270 \times 180$  B-spline knot spans, but of different

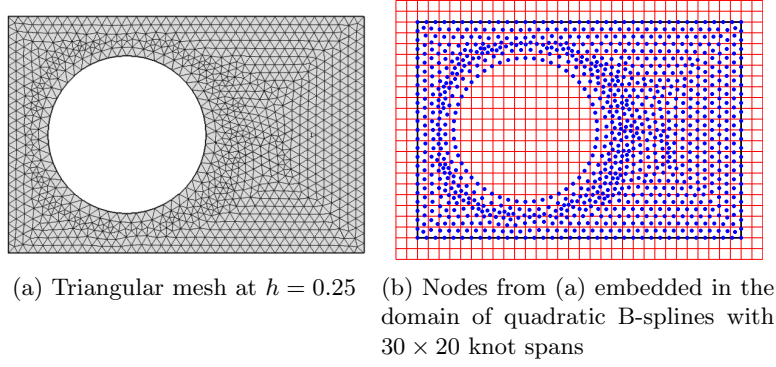


Figure 22: Embedding triangular mesh nodes for the two design domains in Fig. 21 into the domain of B-spline density function for subsequent density evaluation.

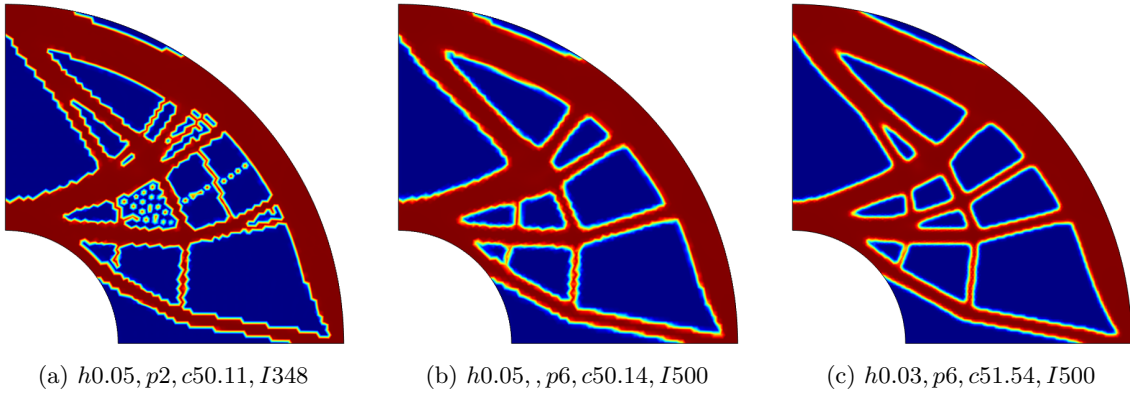


Figure 23: Optimized circular beam parameterized with  $D150 \times 150$  B-spline knot spans and analyzed with triangular linear elements



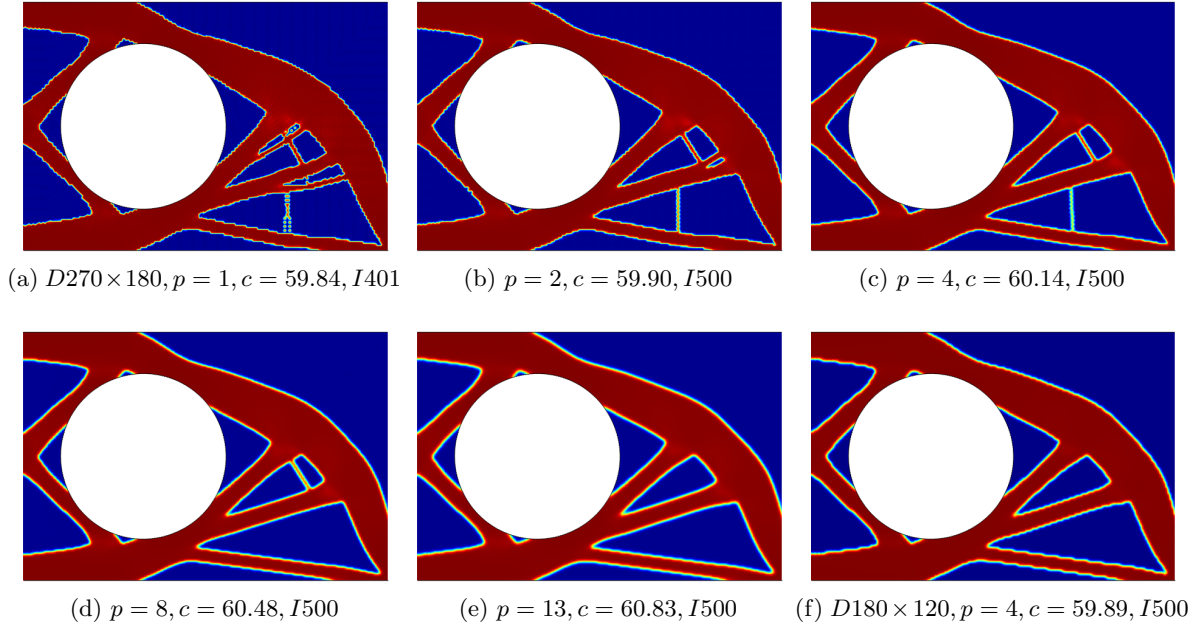


Figure 24: Topology optimization of the cantilever beam with a hole via triangular elements

degrees. As the degree increase, the checkerboard initially appeared in Fig. 24a disappear and the small features disappear. The increased B-spline degree also leads to larger compliance. An alternative to removing checkerboard and filtering smaller features is through reducing the number of knot spans. Figure 24f shows the design optimized with degree 4 B-splines of  $180 \times 120$  spans. Comparing the design with the one in Fig. 24a, checkerboard disappears due to the use of fewer knot spans. Comparing it with the design in Fig. 24c, smaller features in Fig. 24c also disappear.

For better illustration of the density representation in our approach, Fig. 25 shows the density distribution for optimized designs in Fig. 23c and Fig. 24f. The first column in the figure shows the B-spline coefficients. The inactive design variables with zero sensitivity for cost function and volume constraint are in gray color. The second column in the Fig. 25b shows the density distribution in the B-spline domain  $\bar{\Omega}$ . The last column in Fig. 25c shows the density distribution  $\tilde{\rho}(x, y)$  in the design domain with  $(x, y) \in \Omega$ .

## 6.2 Topology optimization of curved domains with isogeometric analysis

The two problems with curved domains shown in Fig. 21 are also solved with NURBS based isogeometric analysis where the density at each quadrature point in analysis is evaluated from the B-spline representation of the continuous density function. It should be noted that, due to the use of NURBS to represent the domain boundary in isogeometric analysis, there is no approximation error in geometry even with a coarse mesh.

Figure 26 shows the NURBS representation of the design domain, analysis mesh refinement and Gaussian quadrature points embedded into the parameter domain. Figure 26a shows the initial NURBS representation of the domain (Fig. 21a), consisting of  $2 \times 1$  bi-quadratic elements. The two internal control points respectively for outer circle and inner circle have weights  $w = (2 + \sqrt{2})/4$

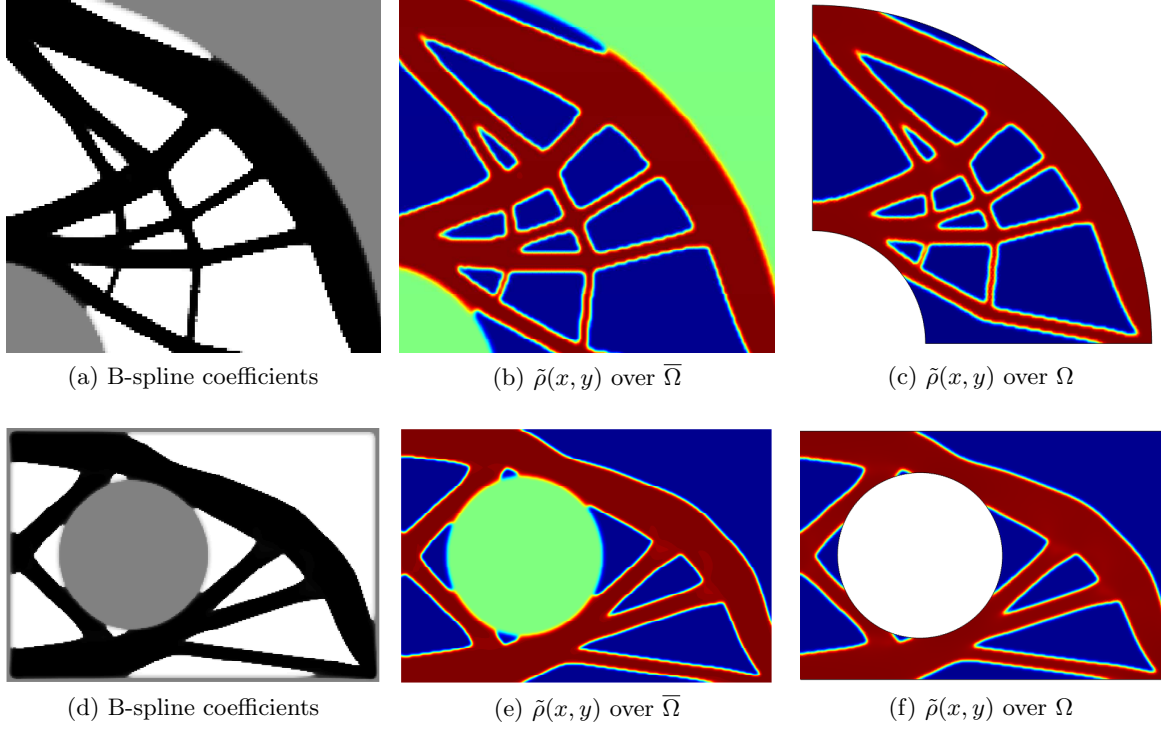


Figure 25: B-spline representation of the density distribution for Fig. 23c and Fig. 24f.

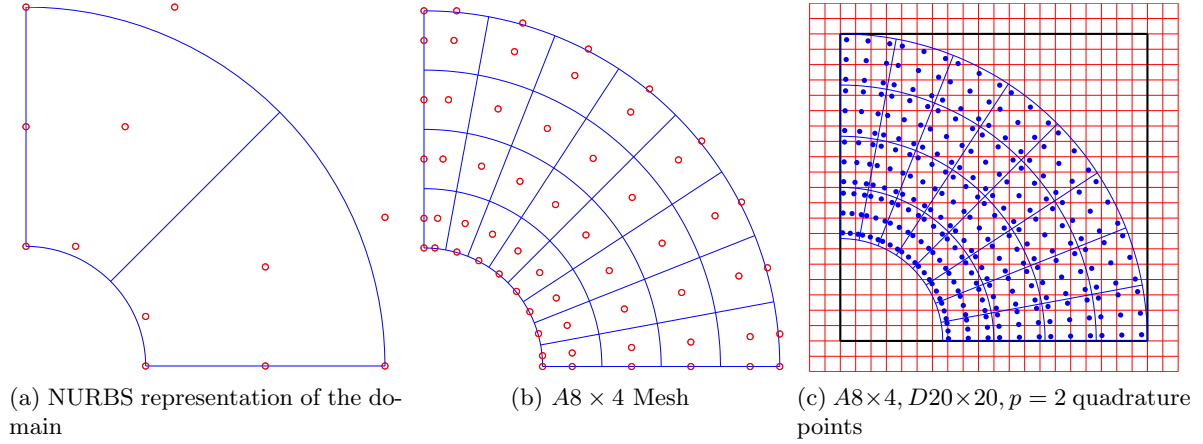


Figure 26: Topology optimization of the curved beam (Fig. 21a) with isogeometric analysis.

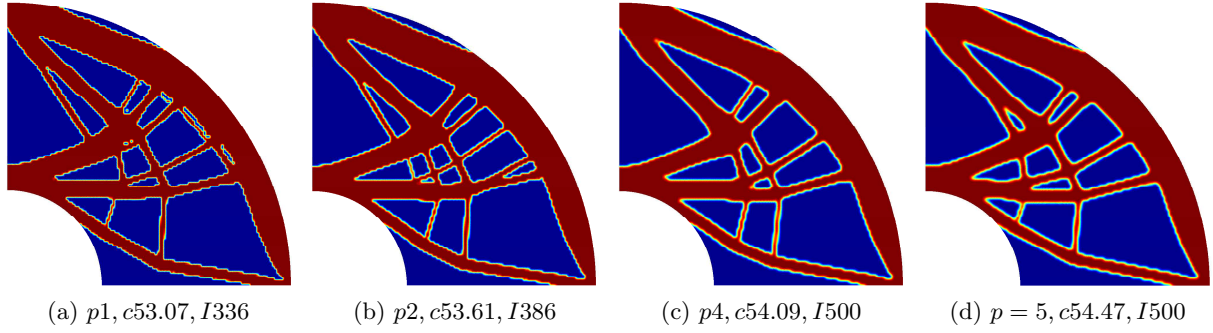


Figure 27: Topology optimization of the circular beam with isogeometric analysis

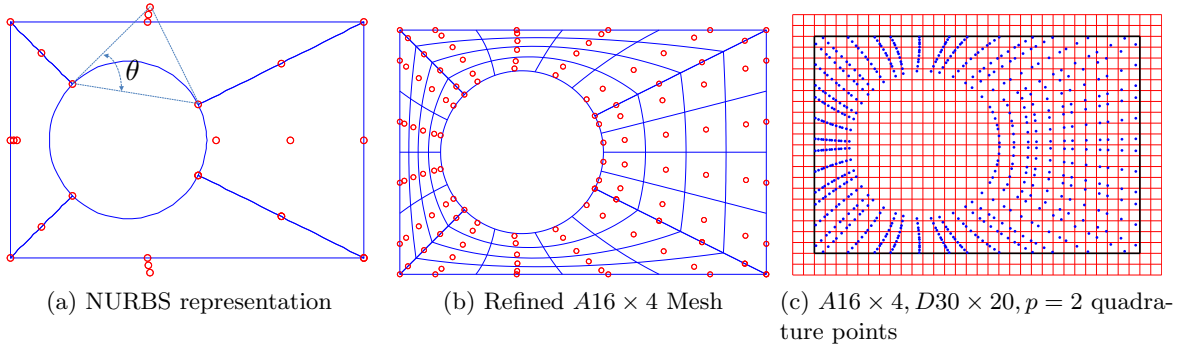


Figure 28: Topology optimization of the cantilever beam (Fig. 21b) with isogeometric analysis

so as to represent the out and inner circles exactly and all other weights are 1. Figure 26b shows refined  $8 \times 4$  NURBS elements. Figure 26c shows the corresponding quadrature points in the domain of bi-quadratic B-spline of  $20 \times 20$  knot spans. For clarity, only coarse mesh and the corresponding quadrature points are shown. The actual mesh and B-spline spans can be much larger in optimization problems. Figure 27 shows optimized design with density parameterized by B-splines and analyzed with biquadratic NURBS elements. The analysis is done by  $128 \times 64$  biquadratic NURBS elements and the B-spline density is parameterized by biquadratic B-splines of  $128 \times 128$  knot spans. From Fig. 27a to Fig. 27d, the B-spline degree increases from  $p = 1$  to  $p = 13$ , the compliance increases and the minimal feature size also increases. This is due to the increased influence region for each B-spline coefficient.

Figure 28 shows the NURBS representation of the design domain and quadrature points in the B-spline domain for the problem in Fig. 21b. Figure 28a shows the bi-quadratic NURBS representation of the domain with design specification in Fig. 21b where the knots in  $\xi$  is  $\{0, 0, 0, 0.25, 0.25, 0.5, 0.5, 0.75, 0.75, 1, 1, 1, \}$  and in  $\eta$  is  $\{0, 0, 0, 1, 1, 1, \}$ . The NURBS weights for four of the control points that represent the circle, but not on the circle are so chosen,  $w = \cos(\theta)$ , that they represent the circular hole exactly. All other weights are 1. Figure 28b shows refined  $16 \times 4$  bi-quadratic NURBS elements. Figure 28c shows the corresponding quadrature points ( $3 \times 3$  per element) on the domain of B-splines. Figure 29 shows the optimized design of the cantilever beam parameterized with B-splines of  $180 \times 120$  knot spans and analyzed with  $128 \times 32$  NURBS elements. As the degree increase from  $p = 2$  to  $p = 10$ , the minimal feature size increases due to the increased influence

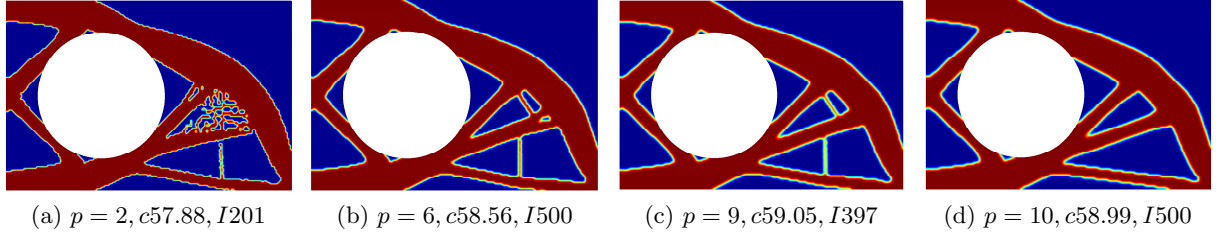


Figure 29: Topology optimization of the cantilever beam parameterized with B-splines of  $180 \times 120$  knot spans and analyzed with  $128 \times 32$  NURBS elements.

region of the B-spline coefficients.

## 7 Conclusions

This paper presents an approach for topology optimization in B-spline space where tensor-product B-splines are used to represent the density field and the density for analysis is then projected from the B-spline based continuous density field. It has been shown that the B-splines provide intrinsic filtering via degrees and knot spans control. Our numerical studies find that, with proper choice of B-spline degrees and knot spans, the design space is free from checkerboards without additional regularization or filtering. Further, B-spline filter is compact, does not require neighboring element information and allows anisotropic length control. Therefore, B-spline filter can be a competitive alternative to the usual density filter, especially when storage cost becomes huge as in 3D problems or when the connectivity of analysis elements is hard to obtain as in mesh-free analysis or in third-part software based analysis.

An exciting opportunity opened up by the topology optimization with B-spline parameterization is the ease of multi-resolution design, leading to efficient exploration of design space. In particular, successive optimization with respect to design resolution leads to topologically simple features obtainable in design representation of different resolutions, thus achieving a form of mesh independency with respect to design resolution.

Future work would also include exploring how B-spline representation can be used in robust formulation [33] to ensure robust control of minimal feature length and how the compactness of B-spline representation can facilitate multi-resolution topology optimization as proposed in [38, 39].

## Acknowledgement

This work is supported in part by the National Science Foundation grant #1200800.

## References

- [1] M. P. Bendsoe and N. Kikuchi. Generating optimal topologies in structural design using a homogenization method. *Computer Methods in Applied Mechanics and Engineering*, 71(2):197–224, 1988.

- [2] M. P. Bendsøe and O. Sigmund. *Topology Optimization: Theory, Methods, and Applications*. Springer Verlag, 2003.
- [3] O. Sigmund and J. Petersson. Numerical instabilities in topology optimization: a survey on procedures dealing with checkerboards, mesh-dependencies and local minima. *Structural and Multidisciplinary Optimization*, 16(1):68–75, 1998.
- [4] G. Allaire, E. Bonnetier, G. Francfort, and F. Jouve. Shape optimization by the homogenization method. *Numerische Mathematik*, 76(1):27–68, 1997.
- [5] T. Borrvall. Topology optimization of elastic continua using restriction. *Archives of Computational Methods in Engineering*, 8(4):351–385, 2001.
- [6] J. Petersson and O. Sigmund. Slope constrained topology optimization. *International Journal for Numerical Methods in Engineering*, 41(8):1417–1434, 1998.
- [7] R. B. Haber, C. S. Jog, and M. P. Bendsøe. A new approach to variable-topology shape design using a constraint on perimeter. *Structural and Multidisciplinary Optimization*, 11(1):1–12, 1996.
- [8] O. Sigmund. On the design of compliant mechanisms using topology optimization. *Journal of Structural Mechanics*, 25(4):493–524, 1997.
- [9] O. Sigmund and K. Maute. Sensitivity filtering from a continuum mechanics perspective. *Structural and Multidisciplinary Optimization*, 46(4):471–475, 2012.
- [10] T. E. Bruns and D. A. Tortorelli. Topology optimization of non-linear elastic structures and compliant mechanisms. *Computer Methods in Applied Mechanics and Engineering*, 190(26 - 27):3443 – 3459, 2001.
- [11] B. Bourdin. Filters in topology optimization. *International Journal for Numerical Methods in Engineering*, 50(9):2143–2158, 2001.
- [12] T. Borrvall and J. Petersson. Topology optimization using regularized intermediate density control. *Computer Methods in Applied Mechanics and Engineering*, 190(37):4911–4928, 2001.
- [13] C. Talischi and G. H. Paulino. An operator splitting algorithm for Tikhonov-regularized topology optimization. *Computer Methods in Applied Mechanics and Engineering*, 253(0):599 – 608, 2013.
- [14] B. S. Lazarov and O. Sigmund. Filters in topology optimization based on Helmholtz-type differential equations. *International Journal for Numerical Methods in Engineering*, 86(6):765–781, 2011.
- [15] A. Kawamoto, T. Matsumori, S. Yamasaki, T. Nomura, T. Kondoh, and S. Nishiwaki. Heaviside projection based topology optimization by a PDE-filtered scalar function. *Structural and Multidisciplinary Optimization*, pages 1–6, 2010. 10.1007/s00158-010-0562-2.
- [16] X. Qian and O. Sigmund. Topological design of electromechanical actuators with robustness toward over-and under-etching. *Computer Methods in Applied Mechanics and Engineering*, 253:237–251, 2012.

- [17] X. Qian and D. Dutta. Physics based B-spline heterogeneous object modeling. In *ASME Design Engineering Technical Conference*, 2001.
- [18] X. Qian and D. Dutta. Physics-based modeling for heterogeneous objects. *ASME Journal of Mechanical Design*, 125(3):416–427, 2003.
- [19] P. Yang and X. Qian. A B-spline-based approach to heterogeneous objects design and analysis. *Computer-Aided Design*, 39(2):95–111, 2007.
- [20] J. Chen and V. Shapiro. Heterogeneous objects modelling and applications. chapter Optimization of continuous heterogeneous models, pages 193–213. Springer-Verlag, Berlin, Heidelberg, 2008.
- [21] X. Y. Kou and S. T. Tan. Heterogeneous object modeling: A review. *Computer-Aided Design*, 39(4):284–301, 2007.
- [22] Y. D. Seo, H. J. Kim, and S. K. Youn. Isogeometric topology optimization using trimmed spline surfaces. *Computer Methods in Applied Mechanics and Engineering*, 199(49-52):3270–3296, 2010.
- [23] L. Dede, M. J. Borden, and T. J. R. Hughes. Isogeometric analysis for topology optimization with a phase field model. *Archives of Computational Methods in Engineering*, 19:427 – 465, 2012.
- [24] A. Kumar and A. Parthasarathy. Topology optimization using B-spline finite elements. *Structural and Multidisciplinary Optimization*, 44(4):471–481, 2011.
- [25] J. Chen, V. Shapiro, K. Suresh, and I. Tsukanov. Shape optimization with topological changes and parametric control. *International Journal for Numerical Methods in Engineering*, 71(3):313–346, 2007.
- [26] V. Braibant and C. Fleury. Shape optimal design using B-splines. *Computer Methods in Applied Mechanics and Engineering*, 44:247 – 267, 1984.
- [27] W. A. Wall, M. A. Frenzel, and C. Cyron. Isogeometric structural shape optimization. *Computer Methods in Applied Mechanics Engineering*, 197:2976 – 2988, 2008.
- [28] X. Qian. Full analytical sensitivities in NURBS based isogeometric shape optimization. *Computer Methods in Applied Mechanics and Engineering*, 199:2059 – 2071, 2010.
- [29] Y. Y. Kim and G. H. Yoon. Multi-resolution multi-scale topology optimization - a new paradigm. *International Journal of Solids and Structures*, 37(39):5529–5559, 2000.
- [30] T. A. Poulsen. Topology optimization in wavelet space. *International Journal for Numerical Methods in Engineering*, 53(3):567–582, 2002.
- [31] L. Piegl and W. Tiller. *The NURBS Book*. Springer-Verlag, New York, 1997.
- [32] G. Farin. *Curves and surfaces for CAGD: a practical guide*. Morgan Kaufmann, 2001.

- [33] F. Wang, B. S. Lazarov, and O. Sigmund. On projection methods, convergence and robust formulations in topology optimization. *Structural and Multidisciplinary Optimization*, 43:767–784, 2011.
- [34] K. Svanberg. The Method of Moving Asymptotes: A new method for structural optimization. *International Journal of Numerical Methods in Engineering*, 24(2):359 – 373, 1987.
- [35] X. Qian and O. Sigmund. Isogeometric shape optimization of photonic crystals via Coons patches. *Computer Methods in Applied Mechanics and Engineering*, 200(25):2237–2255, 2011.
- [36] O. Sigmund. A 99 line topology optimization code written in matlab. *Structural and Multidisciplinary Optimization*, 21:120–127, 2001.
- [37] T. Belytschko, S. P. Xiao, and C. Parimi. Topology optimization with implicit functions and regularization. *International Journal for Numerical Methods in Engineering*, 57(8):1177–1196, 2003.
- [38] T. H. Nguyen, G. H. Paulino, J. Song, and C. H. Le. A computational paradigm for multi-resolution topology optimization (MTOP). *Structural and Multidisciplinary Optimization*, 41(4):525–539, 2010.
- [39] T. H. Nguyen, G. H. Paulino, J. Song, and C. H. Le. Improving multi-resolution topology optimization via multiple discretizations. *International Journal for Numerical Methods in Engineering*, 92:507–530, 2012.